Inorganic Chemistry

pubs.acs.org/IC

Article

Magnetic Properties of High-Nuclearity Fe_x-oxo (x = 7, 22, 24) Clusters Analyzed by a Multipronged Experimental, Computational, and Magnetostructural Correlation Approach

Ashlyn R. Hale, Megan E. Lott, Juan E. Peralta, Dolos Foguet-Albiol, Khalil A. Abboud, and George Christou*

Cite This: *Inorg. Chem.* 2022, 61, 11261−11276

Read Online

ACCESS | Metrics & More | Article Recommendations | Supporting Information

ABSTRACT: The synthesis, structure, and magnetic properties of three related iron(III)-oxo clusters are reported, $[Fe_7O_3(O_2CPh)_9(mda)_3(H_2O)]$ (**1**), $[Fe_{22}O_{14}(OH)_3(O_2CMe)_{21}(mda)_6](ClO_4)_2$ (**2**), and $[Fe_{24}O_{15}(OH)_4(OEt)(O_2CMe)_{21}(mda)_7](ClO_4)_2$ (**3**), where $mdaH_2$ is *N*-methyldiethanolamine. **1** was prepared from the reaction of $[Fe_3O(O_2CPh)_6(H_2O)_3](NO_3)$ with $mdaH_2$ in a 1:2 ratio in MeCN, whereas **2** and **3** were prepared from the reaction of $FeCl_3/NaO_2CMe/mdaH_2$ in a 2:∼13:2 ratio and $FeCl_3/NaO_2CMe/mdaH_2$/pyridine in a 2:∼13:2:25 ratio, respectively, both in EtOH. The core of **1** consists of a central octahedral Fe^{III} ion held within a nonplanar Fe_6 loop by three μ_3-O^{2-} and three μ_2-RO^- arms from the three mda^{2-} chelates. The cores of the cations of **2** and **3** consist of an **A**:**B**:**A** three-layer topology, in which a central Fe_6 (**2**) or Fe_8 (**3**) layer **B** is sandwiched between two Fe_8 layers **A**. The **A** layers structurally resemble **1** with the additional Fe added at the center to retain virtual C_3 symmetry. The central Fe_6 layer **B** of **2** consists of a $\{Fe_4(\mu_4\text{-}O)_2(\mu_3\text{-}OH)_2\}^{6+}$ cubane with an Fe on either side attached to cubane O^{2-} ions, whereas that of **3** has the same cubane but with an $\{Fe_3(\mu_3\text{-}O)(\mu\text{-}OH)\}$ unit attached on one side and a single Fe on the other. Variable-temperature dc and ac magnetic susceptibility studies revealed dominant antiferromagnetic coupling in all complexes leading to ground-state spins of $S = {}^5/_2$ for **1** and $S = 0$ for **2** and **3**. All Fe_2 pairwise exchange parameters (J_{ij}) for **1**−**3** were estimated by two independent methods: density functional theory (DFT) calculations using broken symmetry methods and a magnetostructural correlation previously developed for high-nuclearity Fe^{III}/O complexes. The two approaches gave satisfyingly similar J_{ij} values, and the latter allowed rationalization of the experimental ground states by identification of the spin frustration effects operative and the resultant relative spin vector alignments at each Fe^{III} ion.

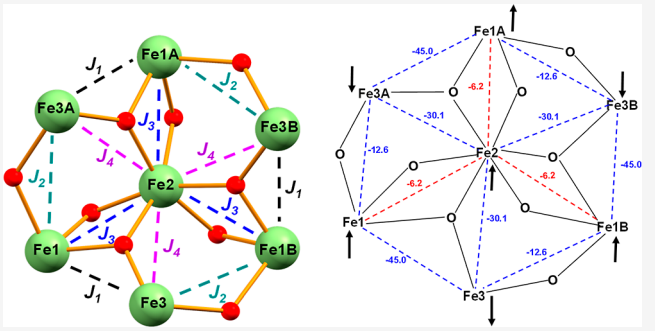

INTRODUCTION

The beauty and utility of Fe^{III}/oxo chemistry in diverse fields such as bioinorganic chemistry, molecular magnetism, and materials science have led to the discovery of a remarkable slew of clusters, spanning nuclearities from Fe_2[1−4] up to giant hexameric $\{Fe_{28}\}_6$ nanocages.[5] Dinuclear Fe^{III} complexes have served as both model systems to understand magnetic exchange couplings via magnetostructural correlations (MSCs)[6] as well as synthetic analogues of di-iron biomolecules such as ribonucleotide reductase,[7,8] hemerythrin,[9] and the soluble methane monooxygenase,[8,10] among others.[11] Higher-nuclearity Fe^{III}/oxo clusters are likewise highly coveted as potential models of intermediates in the growth of nanoscale $Fe^{III}/O/OH$ units during the loading of the ferritin protein,[12] as well as new magnetic molecules and single-molecule magnets (SMMs).[13−18]

Large, discrete $Fe^{III}/O^{2-}/OH^-$ clusters remain highly prized since nuclearities >12 are rare despite considerable efforts over many years. In fact, the family of large $Fe^{III}/O^{2-}/OH^-$ clusters with $n \geq 14$ only numbers 20 members, of which only 4 have $n > 19$.[19−21] Thus, there is still a great need for new synthetic routes to discrete, high-nuclearity $Fe^{III}/O^{2-}/OH^-$ clusters. One fruitful strategy in our group and others has been the use of polyalcohol chelating/bridging ligands in reactions with various Fe^{III} salts or small Fe/oxo complexes, both in the presence and absence of carboxylates.[19,20,22−25] For example, with *N*-methyldiethanolamine ($mdaH_2$), this gave $[Fe^{III}_{22}O_{14}(OH)_3(O_2CMe)_{21}(mda)_6]^{2+}$[19] and $[Fe_7O_3(O_2C^tBu)_9(mda)_3(H_2O)_3]$[25] from the reaction with Fe^{III} salts in the presence of $MeCO_2^-$ or with $[Fe_3O$-

Received: April 22, 2022
Published: July 11, 2022

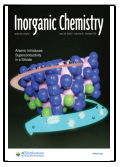

https://doi.org/10.1021/acs.inorgchem.2c01371
Inorg. Chem. 2022, 61, 11261−11276

Table 1. Crystal Data and Structure Refinement Parameters for 1, 2, and 3

parameter	1	2·x(solv)	3·x(solv)
formula[a]	$C_{78}H_{80}Fe_7N_3O_{28}$	$C_{96}H_{202}Cl_2Fe_{22}N_6O_{91}$	$C_{87}H_{170}Cl_2Fe_{24}N_7O_{86.5}$
FW, g mol^{-1}	1898.40	4192.24	4109.59
space group	$Pa\bar{3}$	$C2/c$	$P\bar{1}$
a, Å	24.9810(5)	29.719(3)	13.8505(7)
b, Å	24.9810(5)	35.321(4)	21.9456(12)
c, Å	24.9810(5)	30.651(3)	25.7420(14)
α, deg	90	90	81.118(2)
β,deg	90	98.367(2)	76.501(2)
γ, deg	90	90	80.534(2)
V, Å^3	15589.4(5)	31832(6)	7449.6(7)
λ, Å[b]	0.71073	0.71073	0.71073
Z	8	8	2
T, K	173(2)	173(2)	100(2)
ρ_{calc}, g/cm^3	1.618	1.751	1.832
R_1[c,d]	0.0463	0.0680	0.0424
wR_2[e]	0.1166	0.1581	0.0954

[a] x(solv) is $4H_2O{\cdot}4EtOH{\cdot}4Et_2O$ for **2**, and $^3/_2Et_2O{\cdot}EtOH$ for **3**. [b] Including solvent molecules. [c] $I > 2\sigma(I)$. [d] $R_1 = \sum(||F_o| - |F_c||)/\sum|F_o|$. [e] $wR_2 = [\sum[w(F_o^2 - F_c^2)^2]/\sum[w(F_o^2)^2]]^{1/2}$, $w = 1/[\sigma^2(F_o^2) \pm (m \times p)^2 + n \times p]$, $p = [\max(F_o^2,0) + 2F_c^2]/3$; m and n are constants.

$(O_2C^tBu)_6(H_2O)_3]^{1+}$, respectively. For over 15 years, the former was the largest $Fe^{III}/O/OH$ cluster in the literature until the report in 2019 of a Fe_{34} cluster.[21]

Since oxo-bridged high-spin Fe^{III} ($S = {}^5/_2$) pairs almost always exhibit antiferromagnetic (AF) exchange couplings, high-nuclearity clusters are often replete with spin frustration effects if triangular AF Fe_3 subunits are present, as they usually are. Spin frustration here follows the definition preferred by molecular chemists as the occurrence of competing exchange interactions, J_{ij}, of comparable magnitude that hinder (i.e., frustrate) the preferred spin alignments.[26] As a result, spin frustration often leads to uncompensated ground-state spin, and if the latter is large enough, the Fe_n cluster may even function as an SMM, although Fe^{III} clusters typically do not possess substantial magnetic anisotropy.[27]

In the past, exchange interactions, J_{ij}, in such high-nuclearity Fe^{III}/O clusters have been difficult to determine with confidence from experimental or computational methods owing to (i) the multitude of inequivalent J_{ij} frequently observed as the metal nuclearity increases, (ii) the lack of a reliable MSC for high-nuclearity Fe^{III}/O clusters that could provide reliable estimates of J_{ij} from the metric parameters, and (iii) the increasing computational demands of theoretical methods as nuclearity increases. It was for reason (ii) that our group reported the Mitchell-Christou semiempirical polynuclear Fe^{III}/O MSC procedure in 2016,[28] which enables the calculation of reliable, realistic J_{ij} values in high-nuclearity Fe^{III}/O clusters. The provided protocol also critically accounts for multiple types of oxo-bridging pathways between Fe^{III}_2 pairs, a common occurrence in the Fe^{III}/O architecture of increasingly larger complexes.[28]

The MSC approach coupled with the continually improving power of computational methods and experimental magnetic susceptibility measurements now provide a realistic opportunity to better understand the nature of the various exchange couplings within high-nuclearity Fe^{III}/O clusters from a three-pronged approach involving MSC, density functional theory (DFT), and experimental magnetochemistry methods. While application of three-pronged approaches is common in smaller-nuclearity systems up to Fe_{12} or so,[26c,29,30] our objective more recently has been to tackle clusters of a higher nuclearity at which a detailed study of the exchange couplings and the resulting origin of the magnetic properties is almost nonexistent. In the present work, we report a three-pronged approach to the study of three Fe_x clusters, the new $[Fe_7O_3(O_2CPh)_9(mda)_3(H_2O)]$ (**1**), previously reported $[Fe_{22}O_{14}(OH)_3(O_2CMe)_{21}(mda)_6]$-$(ClO_4)_2$ (**2**) mentioned above, and the newly discovered $[Fe_{24}O_{15}(OH)_4(OEt)(O_2CMe)_{21}(mda)_7](ClO_4)_2$ (**3**); Fe_7 complex **1** is a structural subunit of the larger clusters. We herein report (a) the syntheses of **1** and **3**, (b) the results from a detailed study of the exchange-coupling (J_{ij}) parameters of **1**−**3** by broken symmetry DFT calculations and use of the polynuclear MSC method, (c) the J_{ij} parameters for **1** from fits of experimental $\chi_M T$ versus T data using the program PHI,[31] and (d) the analysis and rationalization of both the spin frustration effects operative and the resulting experimentally determined ground-state spins of **1**−**3**.

EXPERIMENTAL SECTION

Syntheses. All manipulations were performed under aerobic conditions. Reagent grade solvents were used without further purification. Organic reagents were used as received, and $[Fe_3O(O_2CPh)_6(H_2O)_3](NO_3)$ was prepared as described elsewhere;[32] $mdaH_2$ = *N*-methyldiethanolamine.

$[Fe_7O_3(O_2CPh)_9(mda)_3(H_2O)]$ (1). To a stirred orange solution of $[Fe_3O(O_2CPh)_6(H_2O)_3](NO_3)$ (0.50 g, 0.49 mmol) in MeCN (25 mL) was added $mdaH_2$ (0.21 g, 1.8 mmol), causing the solution color to turn brown. The solution was stirred for a further 4 h and filtered, and the sealed filtrate was maintained undisturbed at ambient temperature. Brown plate crystals of **1** slowly grew over a few days and were either maintained in the mother liquor for single-crystal X-ray crystallography or collected by filtration, washed with MeCN, and dried in vacuo for other studies. The yield was 0.095 g (24% based on Fe). The vacuum-dried material was analyzed as **1**·H_2O. Anal. Calcd (found) for $C_{78}H_{82}Fe_7N_3O_{29}$: C, 48.89 (48.64); H, 4.31 (4.36); N, 2.19 (2.59). Selected IR data (KBr disk, cm^{-1}): 3418 (b, m), 2971 (m, sh), 2989 (m, sh), 2860 (m, sh), 1599 (s, sh), 1557 (s, sh), 1519 (m, sh), 1498 (m, sh), 1447 (m sh), 1401 (s), 1262 (w, sh), 1175 (m, sh), 1104 (m), 1061 (m, sh), 1025 (m, sh), 999 (m, sh), 900 (m, sh), 865 (m, sh), 833 (w, sh), 760 (w), 719 (s), 686 (s, sh), 673 (s, sh), 618 (m, sh), 580 (m), 530 (m), 466 (m).

$[Fe_{22}O_{14}(OH)_3(O_2CMe)_{21}(mda)_6](ClO_4)_2$ (2). The procedure below is an improvement to the one reported previously.[19] To a

https://doi.org/10.1021/acs.inorgchem.2c01371
Inorg. Chem. 2022, 61, 11261−11276

stirred solution of $FeCl_3·6H_2O$ (0.30 g, 1.1 mmol) and NaO_2CMe (0.60 g, 7.3 mmol) in EtOH (10 mL) was added $mdaH_2$ (0.14 g, 1.1 mmol), giving rise to a rapid color change from bright orange to dark red-orange. To this solution, $NaClO_4$ (0.07 g, 0.57 mmol) was added, and then the solution was stirred for 15 min. A colorless precipitate was removed by filtration and discarded. Dark red-orange crystals grew over 4 weeks after layering the filtrate with Et_2O, and these were collected by filtration, washed with Et_2O, and dried in vacuo. The vacuum-dried material was analyzed as **2**·$4H_2O$. Anal. Calcd (found) for $C_{72}H_{140}Cl_2Fe_{22}N_6O_{83}$: C, 23.26 (23.55); H, 3.80 (3.75); N, 2.26 (2.00). The yield was 0.037 g (20% based on Fe). Crystals suitable for X-ray crystallography were grown in small vials and maintained in mother liquor until mounted for data collection. Selected IR data (KBr disk, cm^{-1}): 3420 (b, m), 2972 (m, sh), 2926 (m, sh), 2867 (m, sh), 2361 (w, sh), 2337 (w, sh), 1576 (v.st, sh), 1540 (v.st, sh), 1436 (v.st, sh), 1351 (w, sh), 1277 (w, sh), 1248 (w, sh), 1096 (st, sh), 1025 (m, sh), 999 (m, sh), 903 (m, sh), 876 (m, sh), 761 (w, sh), 708 (w, sh), 654 (m, sh), 623 (m, sh), 583 (st, sh), 538 (st, sh), 428 (m).

$[Fe_{24}O_{15}(OH)_4(OEt)(O_2CMe)_{21}(mda)_7](ClO_4)_2$ (3). To a stirred solution of $FeCl_3·6H_2O$ (0.30 g, 1.1 mmol) and NaO_2CMe (0.60 g, 7.3 mmol) in EtOH (10 mL) was added $mdaH_2$ (0.14 g, 1.1 mmol) giving rise to a rapid color change from bright orange to dark red-orange. Pyridine (1.0 mL, 12.4 mmol) was added followed by $NaClO_4$ (0.07 g, 0.57 mmol), and then the solution was stirred for 15 min. The colorless precipitate was removed by filtration and discarded. Dark red-orange crystals grew over 6 weeks after layering the filtrate with Et_2O, and these were collected by filtration, washed with EtOH, and dried in vacuo. The vacuum-dried material was analyzed as **3**·5EtOH. Anal. Calcd (found) for $C_{89}H_{179}Cl_2Fe_{24}N_7O_{89}$: C, 25.56 (26.17); H, 4.31 (3.84); N, 2.34 (2.66). The yield was 0.038 g (20% based on Fe). Crystals suitable for X-ray crystallography were grown in small vials and maintained in mother liquor until mounted for data collection. Selected IR data (KBr disk, cm^{-1}): 3394 (b, m), 2972 (m, sh), 2926 (m, sh), 2867 (m, sh), 2677 (w, sh), 1552 (v.st, sh), 1428 (v.st, sh), 1370 (w, sh), 1288 (w, sh), 1241 (w, sh), 1094 (st, sh), 1024 (m, sh), 999 (m, sh), 902 (m, sh), 876 (m, sh), 760 (w, sh), 712 (w, sh), 655 (m, sh), 634 (m, sh), 583 (st, sh), 534 (st, sh), 431 (m).

X-ray Crystallography. The structures were refined using full-matrix least-squares cycles. The non-H atoms were refined with anisotropic displacement parameters, and all H atoms were placed in calculated, idealized positions and refined riding on their parent atoms. The refinements were carried out by minimizing the wR_2 function using F^2 rather than F values. R_1 was calculated to provide a reference to the conventional R value, but its function was not minimized. Crystal data and refinement parameters are collected in Table 1.

For **1** and **2**·$4H_2O$·4EtOH·$4Et_2O$, data were collected at 173 K on a Siemens SMART PLATFORM equipped with a CCD area detector and a graphite monochromator utilizing Mo Kα radiation (λ = 0.71073 Å). For **1**, the cell parameters were refined using 8192 reflections. A full sphere of data (1850 frames) was collected using the ω-scan method (0.3° frame width). The first 50 frames were remeasured at the end of data collection to monitor instrument and crystal stability (maximum correction on I was < 1%). Absorption corrections by integration were applied based on measured indexed crystal faces. The structure was solved by direct methods in SHELXTL18.[33] The asymmetric unit consists of a $^1/_3$ Fe_7 cluster with two disorders: (i) The C13 benzoate Ph ring displays a resolved twofold rotational disorder with 58:42% occupancies and atom C14 common to both rings; (ii) The second disorder involves the C21 benzoate ligand being a bidentate chelate on Fe3 in one instance and a monodentate ligand in the other with a H_2O (O8) ligand at the second coordination site. The occupancies were 2:1 corresponding to the overall formula $[Fe_7O_3(O_2CPh)_9(mda)_3(H_2O)]$. To check that this disorder is not introduced by choosing the higher symmetry space group $Pa\bar{3}$, the structure was refined in the non-centrosymmetric space group as well as the orthorhombic space group $Pbca$. In both cases, the disorders were observed, thus proving that $Pa\bar{3}$ is the correct space group. A total of 366 parameters were refined in the final cycle of refinement using 5590 reflections with $I > 2\sigma(I)$ to yield R_1 and wR_2 of 4.63 and 11.66%, respectively.

For **2**·$4H_2O$·4EtOH·$4Et_2O$, a preliminary search of reciprocal space revealed a set of reflections with a monoclinic lattice. Initial choice of space group $C2/c$ was subsequently confirmed by the successful solution of the structure. The asymmetric unit consists of the Fe_{22} cluster, two ClO_4^- anions, and four each of H_2O, EtOH, and Et_2O solvent molecules. Charge balance considerations require a +2 charge on the cluster to counter the two ClO_4^- anions in the asymmetric unit, and after bond valence sum calculations on both metals and ligands and close examination of the bond lengths, it was concluded that there is a proton situated on O28. This proton could not be located in a difference Fourier map however, and it was not included in the final refinement. A total of 1618 parameters were refined in the final cycle of refinement using 7571 reflections with $I > 2\sigma(I)$ to yield R_1 and wR_2 of 6.80 and 15.81%, respectively.

For **3**·$^3/_2Et_2O$·EtOH, data were collected at 100 K on a Bruker Dual micro source D8 Venture diffractometer and a PHOTON III detector running the APEX3 software package of programs and using Mo Kα radiation (λ = 0.71073 Å). The data frames were integrated, and multiscan scaling was applied in APEX3. Intrinsic phasing structure solution provided all non-H atoms.[22] The asymmetric unit consists of the Fe_{24} cluster, two ClO_4^- counterions, two Et_2O solvent molecules, one of which is disordered and refined in three parts, and an EtOH molecule disordered over two positions. In the final cycle of refinement, 53,101 reflections [of which 42,129 are observed with $I > 2\sigma(I)$] were used to refine 1952 parameters, and the resulting R_1, wR_2, and S (goodness of fit) were 4.24%, 9.54%, and 1.040, respectively.

DFT Calculations. DFT calculations were performed for **1** and the cations of **2** and **3** using single-crystal X-ray crystallographic coordinates. We considered a total of 12, 62, and 68 distinct J_{ij} first-neighbor exchange couplings for **1** and the cations of **2** and **3**, respectively. These couplings were determined from DFT calculations by mapping broken-symmetry solutions to Ising-type spin configurations $\{S\}$. These configurations were chosen as one high-spin, all single-spin inversions, and all first-neighbor two-spin inversions, giving a total of 20, 85, and 93 broken-symmetry solutions for **1** and the cations of **2** and **3**, respectively. The energies of these configurations are expressed in terms of a sum over spin interactions (eq 1)

$$E(\{S\}) = E_0 - 2\sum_{\langle ij\rangle} J_{ij} S_i \cdot S_j \tag{1}$$

where $\langle ij\rangle$ stands for all neighboring ij pairs, $S_k = \pm^5/_2$ for Fe^{III}, and E_0 is a constant introduced to match the spin model with the DFT energies.

To determine the exchange couplings, J_{ij}, the energies of all configurations $\{S\}$ resulting from broken spin-symmetry DFT calculations were used to perform a linear fit of the Ising-type energy expression in eq 1. This approach has been successfully used in the literature to determine exchange couplings in multicenter transition metal complexes.[34−36] The R^2 in our case for the linear regression differs from 1 by less than 10^{-6}, which indicates that the magnetization is well localized at the magnetic centers, and thus the broken-symmetry DFT solutions are reliable representations of the Ising-type model configurations. The atomic spin populations from the DFT calculations are consistent with the expected broken spin symmetry configuration for all cases.

All DFT calculations were performed using the hybrid Perdew−Burke−Ernzerhof (PBEh) density functional approximation, which admixes 25% of exact (Hartree−Fock-type) exchange and 75% of PBE exchange. This choice of functional is known to perform well for magnetic exchange couplings,[37] yielding for the particular case of oxo-bridged Fe···Fe couplings an RMS error of approximately 10%, as shown for a set of 11 dinuclear Fe^{III} complexes.[38] Pople's all-electron 6-311+G** basis was used for Fe atoms and the 6-31G** for lighter elements[39] with relativistic effects neglected in all calculations. All broken-symmetry DFT energies were obtained using an in-house version of the Gaussian 16 program[40] that allows for a simple spin

https://doi.org/10.1021/acs.inorgchem.2c01371
Inorg. Chem. 2022, 61, 11261−11276

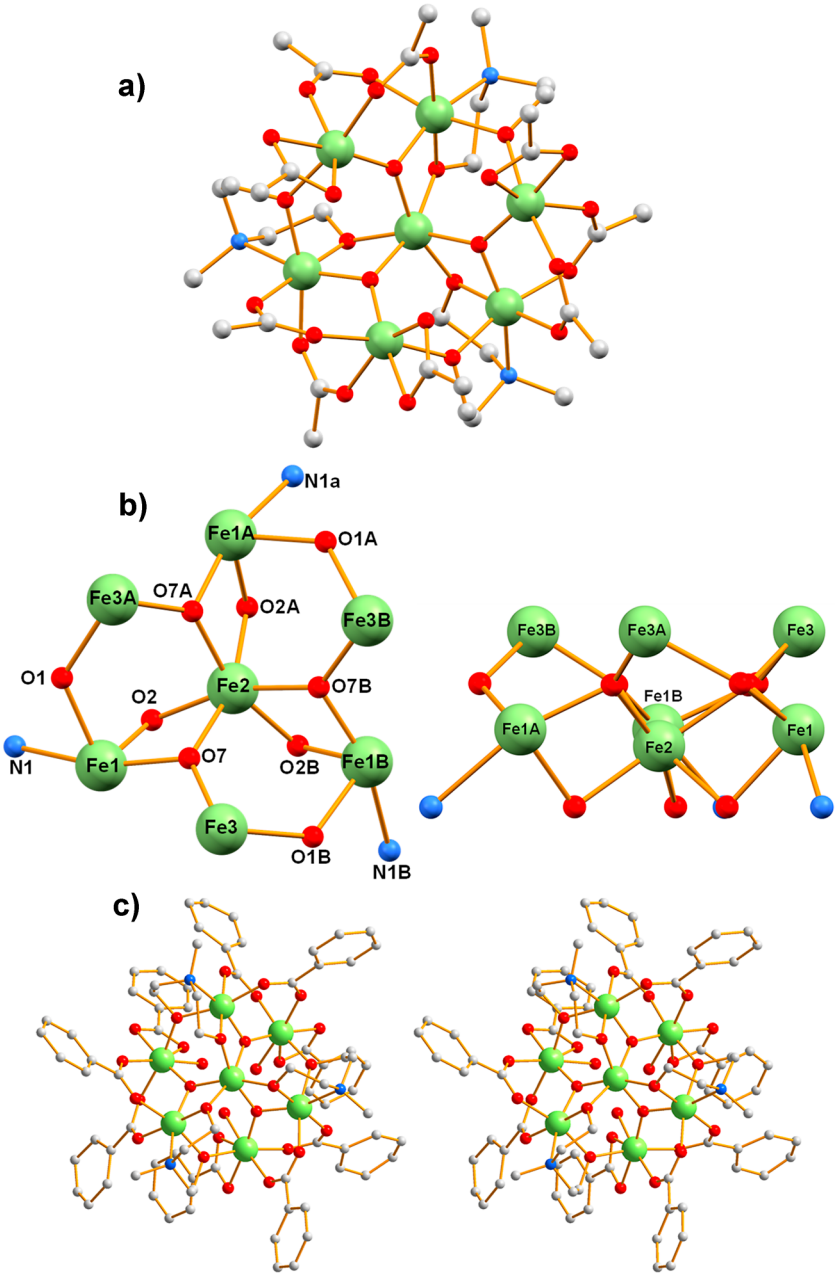

Figure 1. (a) Structure of **1** with all but the *ipso*-C atoms of the Ph rings removed for clarity; (b) labelled core and a side view along the Fe2−Fe1B vector emphasizing the nonplanarity of the Fe_7 unit; and (c) a stereopair of the complete molecule. H atoms are omitted for clarity. Color code: Fe^{III} lime green, O red, N powder blue, C gray.

inversion of the magnetic centers to produce a suitable initial guess for self-consistent calculations. No symmetry was assumed at any point in the model or the DFT calculations. A self-consistency convergence threshold of 10^{-6} Ha = 0.2 cm^{-1} in the energy and 10^{-8} in the RMS changes in the density matrix was used in all calculations.

Other Studies. Infrared spectra were collected in the solid state (KBr pellets) in the 400−4000 cm^{-1} range using a Nicolet Nexus 670 FTIR spectrometer. Direct current (dc) and alternating current (ac) magnetic susceptibility measurements were performed on vacuum-dried polycrystalline solids, embedded in eicosane to prevent torquing, with a Quantum Design MPMS-XL SQUID magnetometer capable of operating with applied dc fields up to 7 T in the 1.8−400 K range. Magnetization vs. field and temperature data were fit using the program MAGNET,[41] and *D* versus *g* fit error surfaces were generated using the program GRID.[42] Pascal's constants were used to estimate the diamagnetic correction,[43] and contributions from the eicosane and gel capsule were measured as a blank. These values were subtracted from the experimental susceptibility to give the molar paramagnetic susceptibility. Dc studies were carried out in the 5.0−300.0 K range in a 0.1 T (1000 Oe) magnetic field and ac studies in the 1.8−15.0 K range in a 3.5 G ac field at an oscillation frequency of 1000 Hz. Elemental analyses (C, H, N) were performed on vacuum-dried samples at Atlantic Microlab, Inc.

RESULTS AND DISCUSSION

Syntheses. Our group's original investigation of the use of $mdaH_2$ in Fe^{III}/O carboxylate chemistry had led to the discovery of **2**[19] and $[Fe_7O_3(O_2C^tBu)_9(mda)_3(H_2O)_3]$ (**4**)[25] from somewhat similar procedures involving the reaction of $mdaH_2$ with $[Fe_3O(O_2CR)_3(H_2O)_3]^+$ salts either preformed or generated in situ from $FeCl_3$/NaO_2CR mixtures. In the present work, we have explored this reaction scheme in more detail,

https://doi.org/10.1021/acs.inorgchem.2c01371
Inorg. Chem. 2022, 61, 11261−11276

concentrating initially on the carboxylate and solvent employed because (i) **2** and **4** are obtained with R = Me and ^{t}Bu, respectively, of significantly different bulkiness, (ii) **2** and **4** are obtained from EtOH and MeCN reaction solvents, respectively, and (iii) the Fe_7 unit of **4** is similar to the Fe_8 units at each end of **2**, differing in the addition of another Fe^{III} (vide infra)—we thus wondered whether the large bulk of ^{t}BuCO$_2^-$ groups was trapping Fe_7 products by shutting down further aggregation to Fe_{22}. We thus employed the R = Ph complex in MeCN in the present work and this again gave an Fe_7 product, complex **1**, with an identical core structure with **4**. When the R = PhCO$_2^-$ and ^{t}BuCO$_2^-$ reactions were instead performed in EtOH, the products were again the Fe_7 products **1** and **4**, respectively, as confirmed by single-crystal unit cell measurements. In contrast, the R = Et reaction in EtOH gave a product that was concluded to be the propionate Fe_{22} cluster from IR spectral comparison with **2**. Thus, it seems that the carboxylate bulk is indeed the determining factor in giving an Fe_7 or Fe_{22} product. This conclusion is rationalized by the space-filling view of the Fe_{22} cation (Figure S1), which shows closely spaced acetate groups in the center of the molecule that could not accommodate larger PhCO$_2^-$ and ^{t}BuCO$_2^-$ groups, thus rationalizing formation instead of **1** and **4**.

The synthesis of **2** involves an excess of mdaH$_2$, and we suspected that it also functions as a base. We thus repeated the reaction with less mdaH$_2$ and/or with added pyridine to see what effect these would have. Small changes in the mdaH$_2$ amount did not change the product, but the presence of an excess of pyridine in the procedure to **2** gave instead Fe_{24} complex **3**. The assembly of the cation is summarized in eq 2. Other bases such as NEt$_3$ also gave **3** but in lower yields.

$$24Fe^{3+} + 21MeCO_2^- + 7mdaH_2 + 49py + 19H_2O + EtOH \rightarrow 49pyH^+ + [Fe_{24}O_{15}(OH)_4(OEt)(O_2CMe)_{21}(mda)_7]^{2+} \quad (2)$$

The reaction time and temperature were also explored. However, when the procedures affording **2** and **3** were run at room temperature for 48 h, at 60 °C for 4 h, and up to 120 °C in a microwave reactor for 1 h, all gave the same products rather than higher-nuclearity species. Similarly, use of phenyldiethanolamine (pdaH$_2$), which was reported to react with [Fe$_3$O(O$_2$C^{t}Bu)$_6$(H$_2$O)$_3$](NO$_3$) in MeCN to yield an analogous Fe_7 cluster to **4**,[44] did not lead to a characterizable product. We note, however, that Baca et al. recently reported a pair of Fe_{22} clusters using ^{i}PrCO$_2$H and either mdaH$_2$ or the ^{n}Bu analogue bdaH$_2$; these Fe_{22} products are similar to **2** but nevertheless significantly different in that they do not have a central {Fe$_4$O$_4$} cubane.[20]

Description of Structures. The complete structure, labeled core, and stereopair of **1** are shown in Figure 1. Selected interatomic distances and angles are listed in Table S1. **1** crystallizes in the trigonal space group $Pa\bar{3}$ with the cluster on a C_3 symmetry axis. The structure consists of a central Fe^{III} (Fe2) held within a nonplanar Fe_6 loop (Fe1, Fe3, and their symmetry partners) by three μ_3-O^{2-} (O7) ions and three μ_2-alkoxide (O2) arms from the three mda^{2-} ligands. All metals are Fe^{III} with near-octahedral geometry, and the deprotonated nature of the bridging O^{2-} and RO$^-$ groups was confirmed by O bond valence sums (Table S2).[45] The Fe1Fe2 pairs are bridged by both O^{2-} and RO$^-$ ions, whereas the Fe3Fe2 pairs are only bridged by O^{2-}, and this will have important consequences for the magnetic properties (vide infra). Peripheral ligation is completed by (i) a chelating mda^{2-} on each Fe1, with one alkoxide arm bridging to the central Fe2 (as mentioned above) and the other bridging to an adjacent Fe3, (ii) a pair of *syn,syn* η^1:η^1:μ-PhCO$_2^-$ ligands bridging each of three symmetry-related Fe1Fe3 pairs, and (iii) a chelating PhCO$_2^-$ ligand on two Fe3 ions, whereas the third Fe3 has a monodentate PhCO$_2^-$ hydrogen-bonded to a terminal H$_2$O (O8) ligand (O8···O10′ = 2.539(5) Å). The resulting disorder about the C_3 axis is described in the Experimental Section.

Complex **2** has been reported elsewhere[19] and is included here for comparison with **3** (vide infra) because their cations are structurally very similar. The complete structure of the cation of **3** as a stereopair and its labeled core are shown in Figure 2, and the selected metric parameters are listed in Table S3. **3** crystallizes in the triclinic space group $P\bar{1}$ with the cation in a general position. Its core consists of three Fe_8 layers with

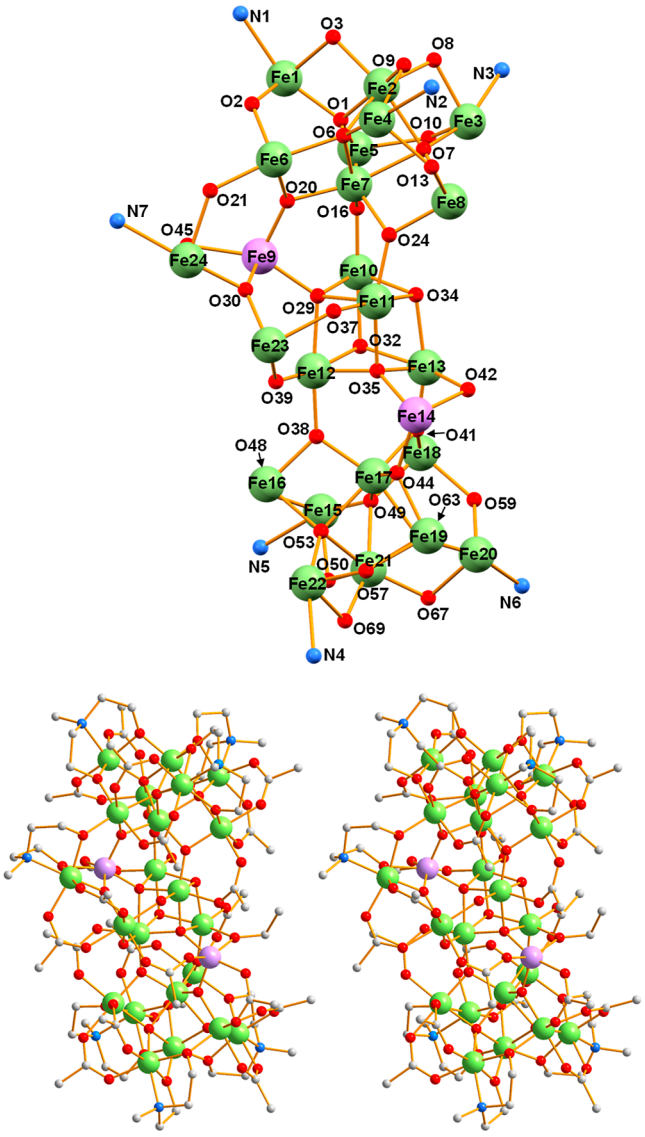

Figure 2. (a) Labelled core of the Fe_{24} cation of **3** and (b) stereopair of the complete cation. H atoms are omitted for clarity. Color code: octahedral Fe^{III} lime green, square-pyramidal Fe^{III} lavender, O red, N powder blue, C gray.

https://doi.org/10.1021/acs.inorgchem.2c01371
Inorg. Chem. 2022, 61, 11261−11276

an **A**:**B**:**A** pattern: the central Fe_8 unit **B** is strikingly asymmetric and comprises an $\{Fe_4(\mu_3\text{-}OH)_2(\mu_4\text{-}O)_2\}^{6+}$ cubane (OH^- ions are O32 and O34) with a triangular $\{Fe_3(\mu_3\text{-}O)\}$ unit (Fe9, Fe23, Fe24) attached on one side via two μ_2-OH^- (O37, O39) ions and cubane O29, and a single Fe (Fe14) on the other side attached via μ_2-OEt^- O42 and cubane O35 (Figures 2 and S2); in the Fe_{22} cation of **2**, the central layer is a more symmetric Fe_6 unit with a single Fe on either side of the cubane (vide infra). Fe^{III} oxidation states and core O protonation levels were confirmed by BVS calculations[45] (Tables S4 and S5, respectively). Twenty-two Fe^{III} are octahedral, while the other two (Fe9 and Fe14) are square-pyramidal; the latter are at the analogous positions as those in **2**.[19] The two Fe_8 units **A** at each end of the cation of **3** are nearly isostructural with a three-blade propeller topology that can be described as essentially the Fe_7 structure of **1**, with an additional Fe atom on the virtual C_3 axis to give the axle (Fe2Fe7 and Fe11Fe21) of each propeller (Figure S2). One Fe_8 unit **A** is connected to the central one by three μ_3-O^{2-} ions (O16/O20/O24), an alkoxide arm (O21) of the unique μ_3-mda^{2-} chelate that has no counterpart at the other end of the molecule, and two μ-$MeCO_2^-$ groups. The other Fe_8 unit **A** is thus connected to the central one by three μ_3-O^{2-} ions (O38/O41/O44) and three μ-$MeCO_2^-$ groups. The peripheral ligation about the cation is completed by the remainder of the μ-$MeCO_2^-$ groups and three μ_3-mda^{2-} chelates on each Fe_8 unit **A**. Interestingly, all $MeCO_2^-$ groups except one bridge in their common *syn,syn* $\eta^1{:}\eta^1{:}\mu$ mode, the exception being the one bridging Fe14Fe23 in the rare *syn,anti* $\eta^1{:}\eta^1{:}\mu$ mode.

Comparison of the Fe_{22} and Fe_{24} Cations. The cations of **2** and **3** are compared in Figure 3 and in the space-filling

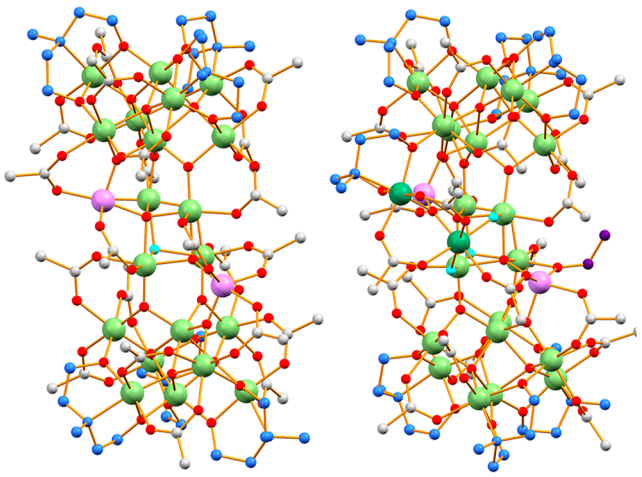

Figure 3. Comparison of the Fe_{22} and Fe_{24} cations of **2** (left) and **3** (right), respectively, using essentially the same viewpoint for **3** as Figure 2. Color code: octahedral Fe^{III} lime green, new octahedral Fe^{III} in **3** dark green, square-pyramidal Fe^{III} lavender, O red, OH^- sky blue, N and C in mda^{2-} ligands powder blue, C in $MeCO_2^-$ gray, and C in EtO^- purple.

mode in Figure S3. They have dimensions of ~1.6 × ~0.7 × ~0.8 nm, excluding C and N atoms. Both possess an **A**:**B**:**A** three-layer topology and are overall fairly similar, with the main differences being in the differing nuclearity of the **B** layer, which are Fe_6 and Fe_8, respectively, and the presence of a seventh mda^{2-} chelate in **3**. The two additional Fe^{III} in **3** (Fe23/Fe24) are shown in darker green in Figure 3 and are located in the $\{Fe_3(\mu_3\text{-}O)\}$ unit attached on one side of the central cubane, as mentioned earlier, with the seventh mda^{2-} chelating on Fe24. As a result, the cation of **3** is distinctly more asymmetric than that of **2**, which has a near-C_2 virtual symmetry, and a root-mean-square deviation (RMSD) analysis gave a weighted RMSD of 0.602 Å (Table S6 and Figure S4) arising from differences in the relative attachment of the **A** layers to the central **B** layer in **3** as well as the structural changes in the central **B** layer caused by incorporation of Fe23 and Fe24. Referring to the viewpoint of Figure 3, the top Fe_8 layer **A** in **2** is near-isostructural with the analogous top layer in **3**, except for a few minor changes to the ligation sphere (Figure 4). However, the bottom Fe_8 layer in **2** is the mirror image of the one in **3** (Figure S5), that is, the orientations of the 'propeller blades' are opposite. In addition, the top and bottom Fe_8 layers **A** are closer to being parallel in **2** than in **3**: for example, the two mean planes through the outermost Fe_3 triangles in each Fe_8 give dihedral angles of 7.21 and 19.44° for **2** and **3**, respectively (Figure S6). This can be assigned to the structural distortions resulting from addition of the seventh mda^{2-} and the extra Fe23/Fe24 ions and their attendant O^{2-}/HO^- ions onto one side of the cation of **3**.

Notwithstanding the differences in the overall structure, the Fe_8 layers **A** of the cations of **2** and **3** are very similar to each other and to the Fe_7 unit in **1**, except that the former two have an extra Fe on the virtual C_3 axis, as mentioned earlier, and some changes to the ligation resulting from attachment to the central layer **B**. The comparison in Figure 4 emphasizes this overall similarity, including in the positions and binding modes of the three mda^{2-} groups. Finally, we note the differences between the cations of **2** and **3** and the Fe_{22} clusters with $^iPrCO_2^-$ by Baca et al.; the latter do not have a cubane in the central layer but instead an $\{Fe_4(\mu_3\text{-}O^{2-})_2\}$ rhombus.[20]

Magnetic Susceptibility Studies. Variable-temperature dc magnetic susceptibility (χ_M) data were collected on crushed vacuum-dried microcrystalline samples in the 5.0−300 K range in a 0.1 T (1 kG) applied dc field and plotted as $\chi_M T$ versus T. For **1**·H_2O, $\chi_M T$ decreases steadily from 6.8 cm^3 K mol^{-1} at 300 K to a nearly constant 4.4 cm^3 K mol^{-1} at 5.0 K (Figure 5a). The 300 K value is much lower than the value for seven noninteracting high-spin Fe^{III} ions with g = 2 (30.6 cm^3 K mol^{-1}), indicating dominant AF interactions. For **3**·5EtOH, $\chi_M T$ decreases steadily from 29.6 cm^3 K mol^{-1} at 300 K to 3.6 cm^3 K mol^{-1} at 5.0 K (Figure 6). The 300 K value is much lower than the 105.0 cm^3 K mol^{-1} (g = 2) value for noninteracting Fe^{III} ions, again indicating dominant AF interactions. This is analogous to the $\chi_M T$ versus T data for **2** (included for comparison in Figure 6), which also exhibits dominant AF interactions.[19]

The near-plateau value for **1**·H_2O at 5.0 K suggests an $S = {}^5/_2$ ground state, and this was supported by ac in-phase (χ_M') magnetic susceptibility data collected in the 1.8 to 15 K range in a 3.5 G ac field with a 1000 Hz oscillation frequency and plotted as $\chi_M' T$ versus T in Figure 5b. The latter exhibited an essentially constant $\chi_M' T \approx 4.5$ cm^3 K mol^{-1} from 15 K down to 1.8 K, confirming only the population of a well isolated $S = {}^5/_2$ ground state in this temperature range. As further confirmation, magnetization (M) versus field (H) and T data were collected in the 0.1−7.0 T and 1.8−10.0 K ranges and plotted as $M/N\mu_B$ versus H/T in Figure 7. The data were fit using the program MAGNET,[41] which assumes that only the ground state is occupied, includes axial zero-field splitting

https://doi.org/10.1021/acs.inorgchem.2c01371
Inorg. Chem. 2022, 61, 11261−11276

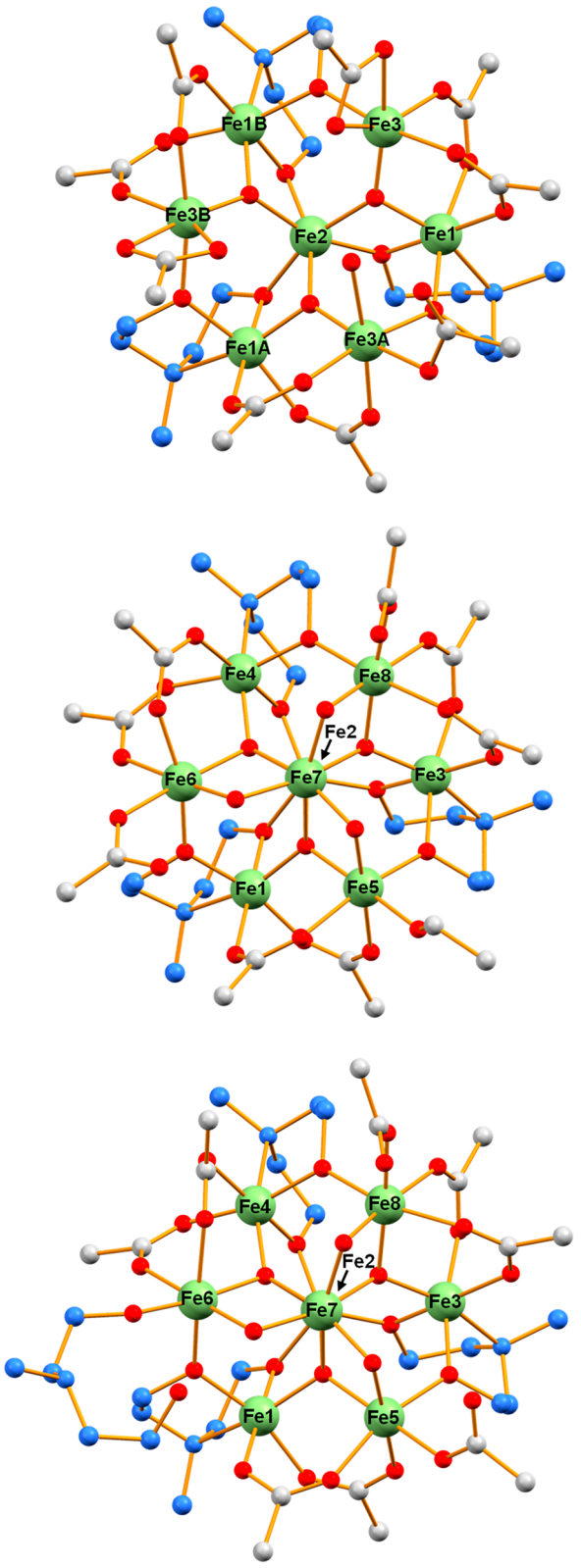

Figure 4. Comparison of **1** with the Fe_8 layers **A** of the cations of **2** and **3**: (a) Fe_7 unit of **1** with all but the *ipso*-C atoms of the Ph rings removed for clarity; (b) Fe_8 layer **A** of **2** in Figure 3 viewed along the Fe2−Fe7 vector; (c) top Fe_8 layer **A** of **3** in Figure 3 viewed along the Fe2−Fe7 vector and including the fourth mda^{2-} chelate. H atoms are omitted for clarity. Color code: octahedral Fe^{III} lime green, O red, C and N atoms of mda^{2-} powder blue, and C gray.

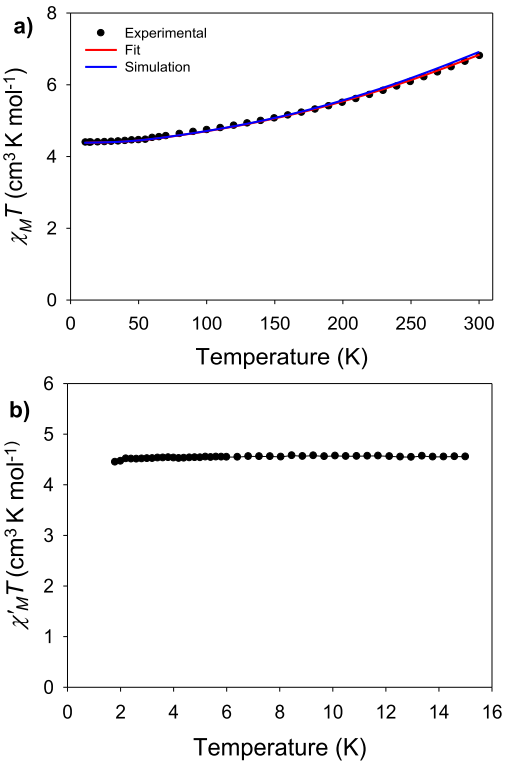

Figure 5. (a) $\chi_M T$ vs T for **1**•H_2O in a 0.1 T dc field. The simulation using the J_{MSC} or J_{DFT} values is shown as a solid blue line, and the J_{PHI} fit as a solid red line; (b) ac in-phase $\chi_M'T$ vs T at a 1000 Hz oscillation frequency.

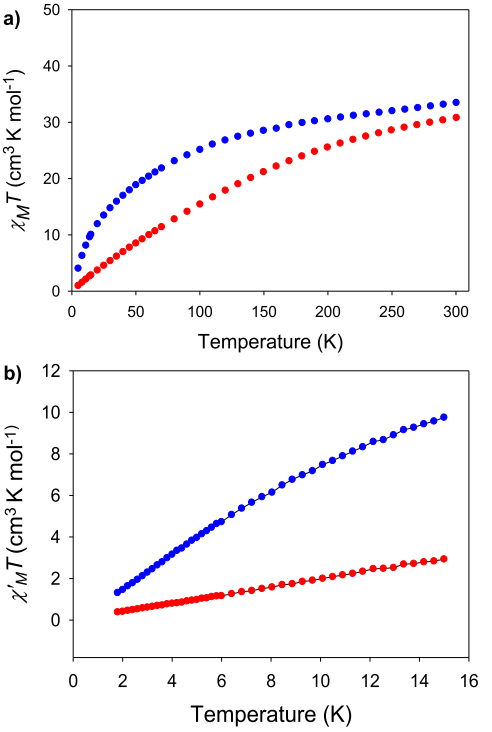

Figure 6. a) $\chi_M T$ vs T in a 0.1 T dc field, and (b) $\chi_M'T$ vs T with a 1000 Hz oscillation frequency for **2**·$4H_2O$ (red ●) and **3**·5EtOH (blue ●).

https://doi.org/10.1021/acs.inorgchem.2c01371
Inorg. Chem. 2022, 61, 11261−11276

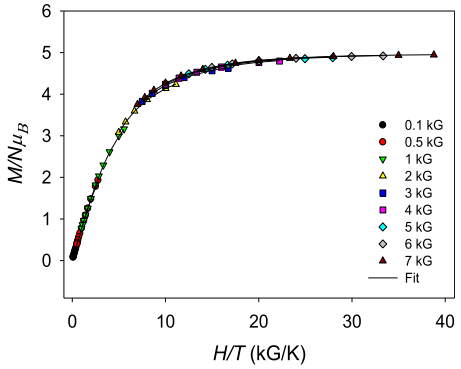

Figure 7. Reduced magnetization ($M/N\mu_B$) vs H/T for **1**•H_2O in the 1.8−10.0 K range at the indicated applied dc fields. The solid lines are the fit of the data; see the text for the fit parameters.

(zfs), $D\hat{S}_z^2$, and the Zeeman interaction, and incorporates a full powder average; the corresponding spin Hamiltonian is given by eq 3.

$$\hat{H} = D\hat{S}_z^2 + g\mu_B\mu_0\hat{S}\cdot H \quad (3)$$

An excellent fit (solid lines in Figure 7) was obtained with $S = {}^5/_2$, $g = 1.99(1)$, and $D = -0.37(3)$ cm^{-1}. As expected, an excellent fit was also obtained with a positive D, giving $S = {}^5/_2$, $g = 1.99(1)$, and $D = +0.45(4)$ cm^{-1}. Both fits are visible in the g versus D error surface generated using the program GRID,[42] and they are of essentially equal quality (Figure S7) with a slightly greater softness in the positive D value. As magnetization fits are not very sensitive to the sign of D, a more sensitive technique such as EPR would be required to reliably determine the sign and magnitude of D.

The dc $\chi_M T$ versus T profile for **3**·5EtOH at low T suggests an $S = 0$ ground state, and this was confirmed by the ac $\chi_M{}'T$ versus T data (Figure 6b), which decreases from 9.1 cm^3 K mol^{-1} at 15.0 K to 1.2 cm^3 K mol^{-1} at 1.8 K clearly heading for zero at 0 K. This is the same as previously reported for **2**·$4H_2O$, whose data are included in Figure 6b for comparison.[19] The decreasing $\chi_M{}'T$ with decreasing T is consistent with low-lying excited states with S greater than the ground state, as expected for a high-nuclearity complex with dominant AF couplings. No out-of-phase $\chi_M{}''$ signals were observed for **1**−**3** (Figure S8).

Ground-State Spin Rationalization Using MSC and DFT Methods. Rationalization of the experimental $S = {}^5/_2$ and $S = 0$ ground states of **1** and the cations of **2** and **3** requires determination of the constituent Fe_2 pairwise exchange coupling parameters, J_{ij}. We thus sought these via two independent methods, a semiempirical MSC developed for high-nuclearity Fe^{III}/O clusters[28] and broken-symmetry DFT calculations. J_{ij} values from the MSC (J_{MSC}) were calculated following the protocol delineated by Mitchell et al.[28] and the use of eq 4, where r is the average Fe−O bond length and φ is the Fe−O−Fe angle

$$J_{ij} = (1.23 \times 10^9)(-0.12 + 1.57\cos\varphi + \cos^2\varphi)\, e^{-8.99r} \quad (4)$$

within each bridged Fe_2 pair. For Fe_2 pairs with multiple monoatomic bridges, the longer average Fe^{III}−O bond was used in accordance with the protocol.[28]

For **1**, J_{MSC} and J_{DFT} are collected in Table 2. The crystallographic C_3 symmetry gives four independent J_{ij} parameters, J_1 and J_2 in the outer Fe_6 loop and J_3 and J_4 to the central Fe2 (Figure 8). The J_1−J_4 determined from the DFT and MSC calculations are satisfyingly in agreement in both sign and magnitude, with the weakest interaction being J_3, as expected for Fe_2 pairs with two monoatomic bridges owing to their smaller Fe−O−Fe angles (96.6 and 99.9°); the other Fe_2 pairs all have only one monoatomic bridge and consequently larger Fe−O−Fe angles (119.5−135.1°). Since all interactions are AF and the Fe_7 topology comprises six edge-fused Fe_3 triangles, the complex is expected to experience spin frustration, here defined in the way most appropriate for molecular systems as competing exchange interactions that prevent (frustrate) the preferred spin vector alignments. J_1 and J_4 are both strong relative to J_2 and J_3, which are intermediate and weak, respectively, so the former two dominate leading to antiparallel alignments both between Fe2 and the Fe3/Fe3A/Fe3B set and between the latter and the Fe1/Fe1A/Fe1B set. This gives an alternating "spin-up, spin-down" alignment pattern around the outer Fe_6 loop corresponding to $m_s = \pm{}^5/_2$ z-components of spin and "spin-up" on the central Fe2 (Figure 8B). This situation also satisfies the J_2 interactions, but the resulting parallel alignments between Fe2 and the Fe1/Fe1A/Fe1B set frustrate J_3 (red dashed lines in Figure 8b), which is AF but much too weak to compete with J_1 and J_4. This is the reason that a "spin-up"/"spin-down" alignment corresponding to $m_s = \pm{}^5/_2$ z-components of spin results, rather than any intermediate spin vector alignments. Thus, the total spin of **1** is $S = {}^{20}/_2 - {}^{15}/_2 = {}^5/_2$, rationalizing the experimentally observed ground state. Note that the same spin vector alignments and the overall $S = {}^5/_2$ are obtained when either the J_{MSC} or J_{DFT} values for J_1−J_4 are used in this analysis.

The J_{MSC} values also give an excellent simulation using the program PHI[31] of the experimental $\chi_M T$ versus T data (blue line in Figure 5a) indicating an $S = {}^5/_2$ ground state and an $S = {}^7/_2$ first excited state at 157 cm^{-1} above it. Interestingly, when the J_{MSC} or J_{DFT} values were used as inputs to fit the data in the

Table 2. Exchange Interactions J_1−J_4 for 1 from MSC Calculations, Broken Symmetry DFT Methods, and PHI Fitting of the Experimental dc Data

J[a]	Fe−O[b]	Fe−O−Fe[b]	J_{MSC}[c]	J_{DFT}[c,d]	J_{PHI}[c,e]	J_0[c,f]	J_{-10}[c,f]	J_{-20}[c,f]
J_1	1.857	119.5	−45.0	−57.0	−28.7(9)	−21.3(3)	−55.6(4)	−23.4(1)
J_2	2.009	128.6	−12.6	−16.3	−30.0(8)	−44.3(8)	−47.4(9)	−56.7(9)
J_3	1.987	96.6	−6.2	−4.9	−13.5(8)	−24.5(8)	+67.5(9)	+24.9(7)
J_4	1.915	135.1	−30.1	−33.4	−42.6(6)	−7.3(8)	−25.7(3)	−40.5(8)
TIP[g]					700	700	700	700

[a]See labeling in Figure 8. [b]Average in Å, and deg. [c]cm^{-1}; $\hat{H} = -2J_{ij}\hat{S}_i\cdot\hat{S}_j$ convention. [d]The DFT calculations gave all J_{ij} values independently, so only one is shown for symmetrically equivalent sets. For J_1 and J_3, all three were identical. For J_2 and J_4, one value differed by 0.1 cm^{-1}. [e]The input values were the MSC values. [f]$J_{\#}$ indicates all J_1−J_4 input values (#) for the fits with PHI. [g]Temperature-independent paramagnetism, ×10^{-6} cm^3 mol^{-1}.

https://doi.org/10.1021/acs.inorgchem.2c01371
Inorg. Chem. 2022, 61, 11261−11276

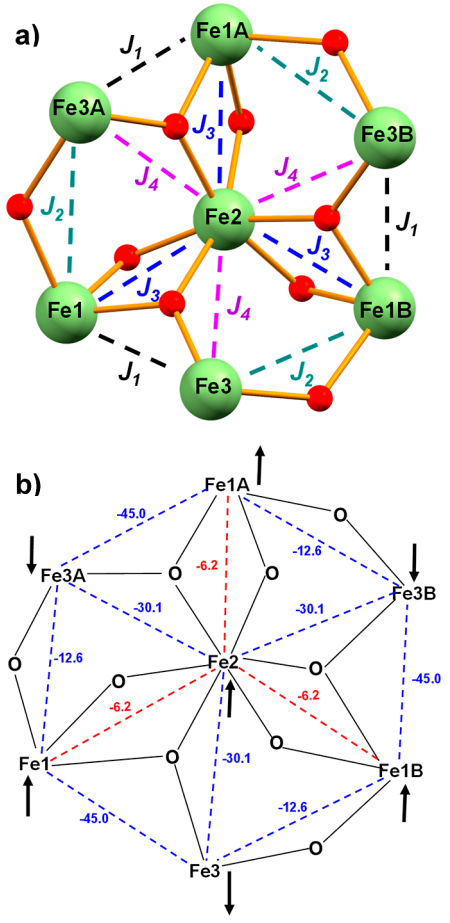

Figure 8. (a) Core of **1** showing the labeling scheme for the constituent exchange interactions. (b) Diagrammatic representation of the core showing the J_{MSC} exchange interactions (cm^{-1}) from Table 2, and the $m_s = \pm^5/_2$ spin alignments predicted by both the J_{MSC} and the J_{DFT} values. Satisfied interactions are blue dashed lines, and frustrated pathways are red dashed lines.

10.0−300 K range (data below 10 K were excluded to avoid effects such as zero-field splitting), a slightly improved fit was obtained (red line in Figure 5a) but with significantly altered J_{PHI} values (Table 2). The fitted J_{PHI} values support the J_{MSC} and J_{DFT} in that J_3 is again the weakest coupling constant, but given the significant changes in absolute values and an apparent "switch" in the values of J_1 and J_4, we suspect that the J_{PHI} fit is an artifact of overparameterization. Thus, since J_{MSC} and J_{DFT} are similar and the simulation is already excellent, we conclude that they are a much better indication of the true J values. As a control, fitting of the data with three other sets of input values were also tested: $J_1 = J_2 = J_3 = J_4 = 0$, −10, or −20 cm^{-1}. Excellent fits were obtained for each, but the J_0, J_{-10}, and J_{-20} values were unreasonable, especially in the strongly AF and/or F values for J_3 (Table 2). We thus conclude that the MSC and DFT approaches provide a synergistic duo of distinct methods for determining the exchange couplings in high-nuclearity Fe^{III}/O clusters where fits of data become unreliable due to overparameterization. We thus now applied them to the Fe_{22} and Fe_{24} cations of **2** and **3**.

To our knowledge, a multipronged analysis using the MSC and theoretical methods of high-nuclearity Fe/O systems has never been attempted before, although the MSC was used in conjunction with experimental fits for complexes of nuclearity up to Fe_{12}.[29a] As there are 62 and 68 symmetry-inequivalent J_{ij} couplings in **2** and **3**, respectively, attempts to fit the experimental $\chi_M T$ versus T data were never considered. Instead, we implemented the MSC and DFT methods to estimate the J_{ij} values and then tried to rationalize the experimentally determined $S = 0$ ground states of both cations by identifying, if possible, spin frustration effects and the resulting spin vector alignments at each Fe^{III}, that is, an analogous analysis to that for **1**. The resulting J_{MSC} and J_{DFT} values for **2** and **3** are collected in Tables 3−5 covering J_{ij} values (i) within the central Fe_8 layers **B**, (ii) at the interface between layers **A** and **B**, and (iii) within the top Fe_8 layers **A**

Table 3. J_{MSC} and J_{DFT} Exchange Interactions in the Top Fe_8 Layer A in the Cations of 2 and 3

	2				3			
J^a	Fe−O[b]	Fe−O−Fe[b]	J_{MSC}[c]	J_{DFT}[c]	Fe−O[b]	Fe−O−Fe[b]	J_{MSC}[c]	J_{DFT}[c]
$J_{1,2}$	1.996	97.5	−6.1	−3.0	1.992	97.2	−6.2	−3.5
$J_{1,5}$	1.930	116.7	−22.4	−30.6	1.961	117.2	−17.1	−23.1
$J_{1,6}$	1.977	129.9	−16.8	−20.3	2.001	127.6	−12.4	−16.8
$J_{1,7}$	2.052	135.9	−8.8	−17.7	1.973	127.6	−17.1	−21.0
$J_{2,3}$	1.995	97.3	−6.0	−2.3	2.011	95.9	−4.7	−0.5
$J_{2,4}$	1.996	97.9	−6.3	−4.5	2.013	95.6	−4.5	+1.1
$J_{2,5}$	2.038	135.2	−9.9	−17.5	2.024	134.4	−11.2	−17.7
$J_{2,6}$	2.052	134.0	−8.8	−15.5	2.07	139.0	−7.5	−14.8
$J_{2,7}$	2.160	82.7	+0.4	+6.0	2.11	83.6	+0.4	+5.9
$J_{2,8}$	2.044	134.7	−9.4	−16.3	2.038	136.4	−10.0	−17.6
$J_{3,5}$	1.991	129.6	−14.9	−19.3	2.005	127.0	−12.9	−18.1
$J_{3,7}$	2.030	136.4	−10.7	−19.5	2.026	134.5	−11.0	−19.2
$J_{3,8}$	1.946	116.3	−19.3	−25.8	1.943	116.7	−19.9	−26.6
$J_{4,6}$	1.964	117.3	−16.6	−23.2	1.978	114.1	−14.1	−20.0
$J_{4,7}$	1.997	129.4	−14.1	−21.4	2.016	136.6	−12.2	−22.1
$J_{4,8}$	1.979	128.8	−16.4	−20.4	1.997	127.9	−13.9	−18.6
$J_{5,7}$	2.094	90.7	−1.1	−1.6	2.036	94.3	−3.2	−3.3
$J_{6,7}$	2.053	92.3	−2.2	−1.4	2.073	91.9	−1.7	−1.7
$J_{7,8}$	2.078	90.4	−1.3	−1.3	2.053	91.9	−2.0	−1.9

[a]See Figure 9. [b]Average in Å, and deg. [c]cm^{-1}; $\hat{H} = -2J_{ij}\hat{S}\cdot\hat{S}$ convention.

https://doi.org/10.1021/acs.inorgchem.2c01371
Inorg. Chem. 2022, 61, 11261−11276

Table 4. J_{MSC} and J_{DFT} Exchange Interactions in the Interface Between the Top and Bottom Fe_8 Layers A and the Central Layer B in the Cations of 2 and 3

	2				3			
J^a	Fe−O[b]	Fe−O−Fe[b]	J_{MSC}[c]	J_{DFT}[c]	Fe−O[b]	Fe−O−Fe[b]	J_{MSC}[c]	J_{DFT}[c]
$J_{5,10}$	1.918	130.9	−28.7	−32.4	1.886	130.1	−38.3	−40.8
$J_{6,9}$	1.880	132.9	−41.0	−43.8	1.891	135.6	−37.2	−41.6
$J_{7,9}$	1.890	125.4	−35.6	−38.0	1.889	120.8	−34.3	−35.5
$J_{7,10}$	1.891	119.7	−33.2	−36.4	1.890	128.0	−36.3	−36.3
$J_{7,11}$	1.901	124.1	−32.1	−36.2	1.911	121.5	−28.4	−31.5
$J_{8,11}$	1.914	127.8	−29.2	−34.1	1.916	132.0	−29.4	−32.5
$J_{12,16}$	1.900	131.2	−33.8	−33.8	1.900	130.8	−33.8	−33.6
$J_{12,17}$	1.892	123.3	−34.3	−37.6	1.901	125.5	−32.5	−32.7
$J_{13,17}$	1.879	127.7	−40.2	−41.4	1.894	121.5	−33.2	−35.0
$J_{13,18}$	1.901	130.9	−33.5	−37.7	1.900	131.6	−34.0	−33.3
$J_{14,17}$	1.880	124.8	−39.0	−42.4	1.897	122.7	−32.8	−37.6
$J_{14,19}$	1.894	132.7	−36.1	−38.6	1.898	127.4	−33.7	−40.6
$J_{6,24}$					2.031	128.2	−10.2	−14.7

[a]See Figures 10 and 11 for 2 and 3, respectively. [b]Average in Å, and deg. [c]cm^{-1}; $\bar{H} = -2J_{ij}\bar{S}\cdot\bar{S}$ convention.

Table 5. J_{MSC} and J_{DFT} Exchange Interactions for Central Layer B in the Cations of 2 and 3

	2				3			
J^a	Fe−O[b]	Fe−O−Fe[b]	J_{MSC}[c]	J_{DFT}[c]	Fe−O[b]	Fe−O−Fe[b]	J_{MSC}[c]	J_{DFT}[c]
$J_{9,10}$	2.048	94.5	−3.0	−0.3	2.018	114.8	−9.8	−14.0
$J_{9,11}$	1.950	141.9	−22.2	−28.9	2.021	120.9	−10.5	−14.7
$J_{9,12}$	2.004	108.9	−9.7	−8.2	2.037	122.6	−9.3	−11.9
$J_{10,11}$	2.102	96.4	−2.2	−3.7	2.104	94.8	−1.8	−2.5
$J_{10,12}$	2.105	102.5	−3.1	−6.1	2.087	100.8	−3.3	−3.5
$J_{10,13}$	2.095	103.4	−3.5	−5.4	2.077	104.0	−4.2	−7.0
$J_{11,12}$	2.086	94.7	−2.1	−1.0	2.083	95.2	−2.3	+0.3
$J_{11,13}$	2.125	101.5	−2.4	−4.4	2.116	100.9	−2.6	−6.3
$J_{11,14}$	2.029	116.4	−9.1	−11.3	1.998	113.5	−11.5	−13.1
$J_{12,13}$	2.082	95.8	−2.5	−2.3	2.095	96.4	−2.3	−1.6
$J_{12,14}$	1.995	128.3	−14.2	−22.8	1.981	138.5	−16.7	−24.6
$J_{13,14}$	2.015	113.8	−9.9	−16.8	2.012	97.8	−5.4	−3.4
$J_{9,23}$					1.897	135.3	−35.4	−39.1
$J_{9,24}$					1.996	95.5	−5.2	−11.6
$J_{11,23}$					1.976	125.7	−16.5	−16.3
$J_{12,23}$					1.964	133.2	−19.2	−20.49
$J_{23,24}$					1.866	121.8	−42.7	−45.4

[a]See Figures 10 and 11 for 2 and 3, respectively. [b]Average in Å, and deg. [c]cm^{-1}; $\bar{H} = -2J_{ij}\bar{S}_i\cdot\bar{S}_j$ convention.

(from the viewpoint of Figure 4), respectively. J_{ij} for the bottom Fe_8 layers **A** are tabulated in Table S7.

Even with such large Fe_{22}/Fe_{24} nuclearity clusters, J_{MSC} and J_{DFT} are in very good agreement in terms of both sign and magnitude. For convenience, we consider J_{ij} to be of three types: weak, intermediate, and strong, with approximate $|J_{ij}|$ of <10 cm^{-1}, ∼10 to ∼25 cm^{-1}, and >25 cm^{-1}, respectively. As stated, $|J_{ij}|$ <10 cm^{-1} are characteristic of Fe_2 pairs with two monoatomic bridges, whereas stronger couplings are expected with only one monoatomic bridge. DFT calculations are on the complete cations and are affected by the total nuclearity, whereas MSC calculations are independent of the nuclearity, being localized at each Fe_2 pair in turn. So, the very satisfying agreement in J_{MSC} and J_{DFT} for essentially every interaction emphasizes the power and utility of the DFT approach even for such complicated systems. The J_{MSC} and J_{DFT} only differ *in sign* for two couplings each in **2** and **3**: J_{MSC}/J_{DFT} for $J_{15,21}$ = −4.9 cm^{-1}/+1.1 cm^{-1} and $J_{17,18}$ = −2.1 cm^{-1}/+0.8 cm^{-1} for **2**, and $J_{2,4}$ = −4.5 cm^{-1}/+1.1 cm^{-1} and $J_{11,12}$ = −2.3 cm^{-1}/+0.3 cm^{-1} for **3**. This sign discrepancy is not surprising given that these couplings are so weak.

Since the top Fe_8 layers **A** are similar to **1**, we shall discuss them first. The J_{MSC} and J_{DFT} values are listed in Table 3, and diagrammatic representations are provided in Figure 9 showing the J_{MSC} locations; note that use of the J_{DFT} values in Figure 9 would lead to the same conclusions reached below. The spin alignments in the Fe_8 propeller unit in **2** and **3** can be determined by identifying the spin frustrated pathways, as was done for **1**. Notwithstanding that the extra central Fe7 forming the axle with Fe2 causes some structural perturbation relative to **1**, a similar spin frustration pattern results between the Fe_8 layer **A** of **2** and **3** and that of **1**, that is, the weakest AF J_{ij} for bis-monoatomically bridged Fe_2 pairs ($J_{1,2}$, $J_{2,3}$, $J_{2,4}$, $J_{5,7}$, $J_{6,7}$, and $J_{7,8}$) is frustrated by the two stronger J_{ij} in each Fe_3 triangular unit, leading to parallel alignments in these Fe_2 pairs as the outer spin vectors align in an antiparallel up-down fashion around the outer hexagon. This also leads to the spin vectors Fe2/Fe7 being aligned antiparallel, which means that $J_{2,7}$ is also frustrated if it really is F, as indeed J_{MSC} and J_{DFT} indicate in

https://doi.org/10.1021/acs.inorgchem.2c01371
Inorg. Chem. 2022, 61, 11261−11276

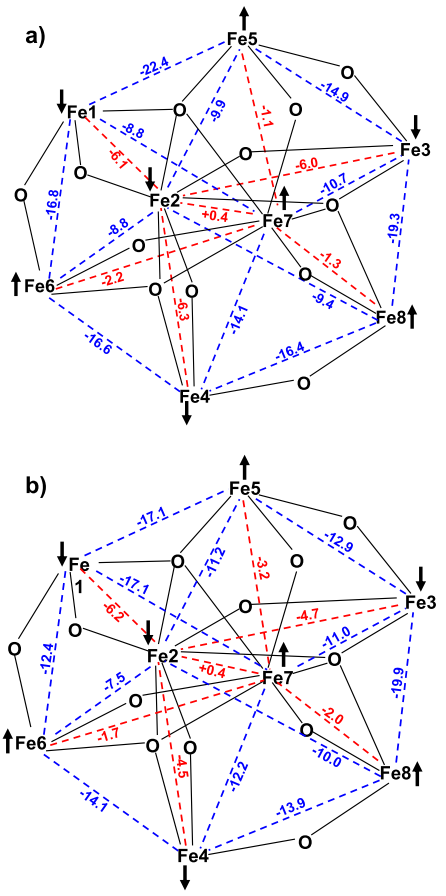

Figure 9. Diagrammatic representation of the cores of the top Fe_8 layer **A** of (a) **2** and (b) **3** showing the J_{MSC} exchange interactions (cm^{-1}) from Table 3, and the $m_s = \pm^5/_2$ spin alignments predicted by both the J_{MSC} and the J_{DFT} values. Satisfied interactions are blue dashed lines, and frustrated pathways are red dashed lines.

both **2** and **3** (Table 3). This is reasonable given that the Fe2/Fe7 axle pair is tris-monoatomically bridged by three μ_4-O^{2-} ions with very acute Fe−O−Fe angles in the 82.7−86.5° range. Overall, the Fe_8 unit is thus predicted to have an $S = 10 - 10 = 0$ ground state. A similar analysis of the bottom Fe_8 layers **A** of **2** and **3** leads to an analogous alignment pattern and a predicted $S = 0$ ground state (Figure S9).

A similar analysis can now be carried out on the interfaces between the layers **A** and the central Fe_6 and Fe_8 layers **B** of the cations of **2** and **3**, respectively, and then on the central layers themselves. We shall describe the former first because the J_{ij} in the central layer are almost all weak so that their spin alignments are strongly dominated by the J_{ij} at the interfaces. J_{MSC} and J_{DFT} at the latter in the cation of **2** (Table 4 and Figure 10) show that all J_{ij} between Fe5,6,7,8 of top layer **A** and Fe9,10,11 of the central layer **B** are strongly AF, and since the spin vectors of the former are all parallel due to the spin frustration effects described above, this aligns the spin vectors of Fe9,10,11 all parallel to each other and antiparallel to those of Fe5,6,7,8, frustrating the weaker AF interactions $J_{9,10}$, $J_{9,11}$, and $J_{10,11}$ (red dashed lines in Figure 10): $J_{9,10}$ and $J_{10,11}$ are very weak (Table 5), as expected for bis-monoatomically bridged Fe_2 pairs, and easily frustrated, whereas $J_{9,11}$ is of intermediate strength ($J_{MSC}/J_{DFT} = -22.2/-28.9$ cm^{-1}) since it has a single monoatomic bridge, but it is competing with the four strong $J_{6,9}$, $J_{7,9}$, $J_{7,11}$, and $J_{8,11}$ in the ranges $J_{MSC} = -29.2$ to -41.0 cm^{-1} and $J_{DFT} = -34.1$ to -43.8 cm^{-1}.

The same situation is seen at the interface of the bottom Fe_8 layer **A** of **2** with the central layer **B**. J_{MSC} and J_{DFT} again show that all J_{ij} between Fe16,17,18,19 of the bottom layer **A** and Fe12,13,14 of the central layer **B** are strongly AF (Table 4 and Figure 10), and since the spin vectors of the former are all parallel, this again aligns the spin vectors of Fe12,13,14 all parallel to each other and antiparallel to those of Fe16,17,18,19, frustrating the weaker AF interactions $J_{12,13}$, $J_{12,14}$, and $J_{13,14}$ (red dashed lines in Figure 10); $J_{12,14}$ is of intermediate strength ($J_{MSC}/J_{DFT} = -14.2/-22.8$ cm^{-1}) (Table 5), but it is competing with the four strong $J_{12,16}$, $J_{12,17}$, $J_{14,17}$, and $J_{14,19}$ in the ranges $J_{MSC} = -33.8$ to -39.0 cm^{-1} and $J_{DFT} = -33.8$ to -42.4 cm^{-1}. The remaining step is to assess the situation in the central Fe_6 layer **B** of **2**, and it is clear from Table 5 that almost all J_{ij} are AF and weak except the two mentioned already, that is, $J_{9,11}$ and $J_{12,14}$. However, even though all J_{ij} between the Fe9,10,11 and Fe12,13,14 planes are weak, they are not competing and thus none are frustrated by the resulting antiparallel alignments of the spin vectors of these two planes (Figure 10).

Comparing now the J_{MSC}/J_{DFT} values for **2** versus **3** in Tables 3−5 leads to the conclusion that the spin vector alignments in the larger Fe_{24} cation of **3** are analogous to those in **2** (Figure 11). The main difference is, of course, the extra Fe23 and Fe24 ions in the now Fe_8 central layer **B**, and these have entered one each into what were the two Fe_3 planes to make them Fe_4. Otherwise, the same pattern of spin vector alignments is seen, that is, strongly AF interactions in the interface region between layers **A** and **B**, frustrating the weaker interactions within the Fe_4 planes and thus leading to parallel and antiparallel spin alignments within and between the Fe_4 planes, respectively. $J_{12,14}$ and $J_{12,23}$ are again of intermediate strength but are nevertheless frustrated by the multiple stronger interactions with which they are competing, $J_{12,16}$, $J_{12,17}$, $J_{9,23}$, and $J_{23,24}$.

The overall picture that emerges is that in all areas of the cations of **2** and **3**, there is complete frustration of one interaction in each Fe_3 triangular unit either because the other two interactions are much stronger, or because strong interactions in neighboring Fe_3 triangular units are enforcing the frustration, or both. In effect, the Fe_3 units are magnetically near-isosceles, and this is primarily due, of course, to the common occurrence in higher-nuclearity Fe^{III}/O clusters of bis-monoatomically bridged Fe_2 pairs giving characteristically very weak J_{ij} values. This also leads in the cations of **2** and **3** to a "spin-up"/"spin-down" alignment of the spin vectors corresponding to $m_s = \pm^5/_2$ z-components of spin, as summarized in Figure 12. The spin alignments described above lead to an $S = 0$ ground state for the three **A**:**B**:**A** layers, and so the overall spin is predicted to be $S = 0$ for both cations, in agreement with the experimental susceptibility data. As a consistency check for the interpretation of the $S = 0$ ground state, we also determined the lowest-energy configuration of the cations of **2** and **3** by explicitly evaluating the 2^{22} and 2^{24} energies given by eq 1 using both the J_{MSC} and J_{DFT} sets of couplings. The resulting lowest-energy configuration was found in all cases to be the same as shown in Figure 12.

CONCLUSIONS

The use of $mdaH_2$ in Fe^{III}/O carboxylate cluster chemistry has led to three products with Fe_7, Fe_{22}, and Fe_{24} nuclearities, the

https://doi.org/10.1021/acs.inorgchem.2c01371
Inorg. Chem. 2022, 61, 11261−11276

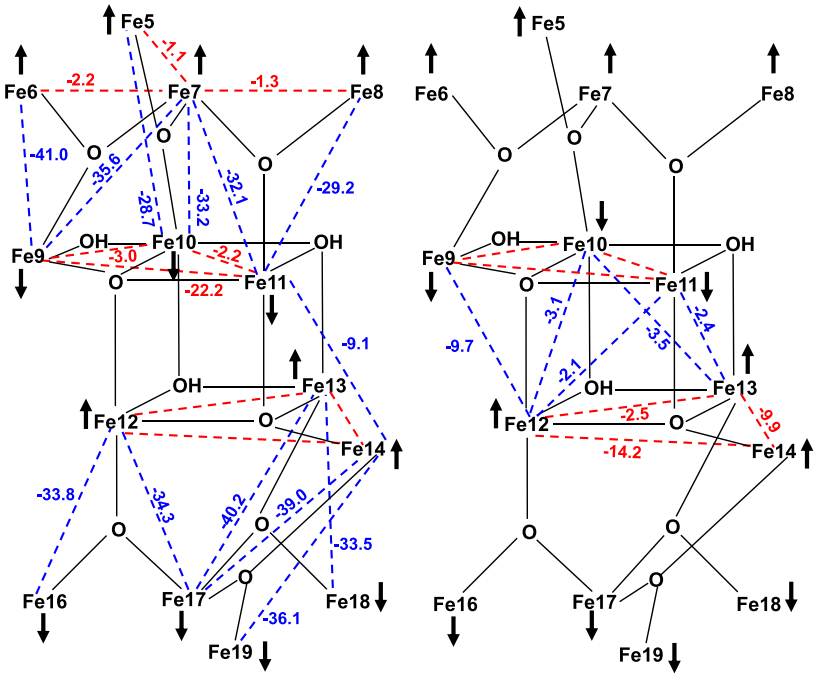

Figure 10. Diagrammatic representation of the core of the central Fe_6 layer **B** of **2** plus selected atoms from the two Fe_8 layers **A**, showing the J_{MSC} exchange interactions (cm^{-1}) from Tables 4 and 5 in (left) the interface regions between **A** and **B** and (right) the central layer **B**. For clarity, $J_{11,14}$ is shown on the left. Also shown are the ground-state $m_s = \pm^5/_2$ spin alignments predicted by both J_{MSC} and the J_{DFT} values. Satisfied interactions are blue dashed lines, and frustrated pathways are red dashed lines.

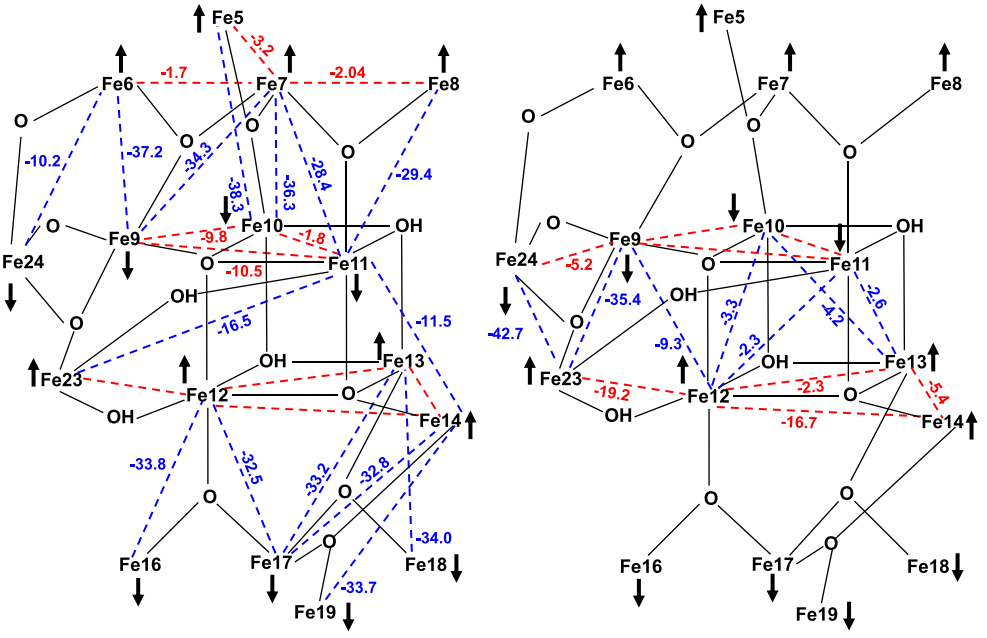

Figure 11. Diagrammatic representation of the core of the central Fe_8 layer **B** of **3** plus selected atoms from the two Fe_8 layers **A**, showing the J_{MSC} exchange interactions (cm^{-1}) from Tables 4 and 5 in (left) the interface regions between **A** and **B** and (right) the central layer **B**. For clarity, $J_{11,14}$ and $J_{11,23}$ are shown on the left. Also shown are the ground-state $m_s = \pm^5/_2$ spin alignments predicted by both J_{MSC} and the J_{DFT} values. Satisfied interactions are blue dashed lines, and frustrated pathways are red dashed lines.

different products resulting from a systematic screening of different carboxylic acids and the presence or absence of additional base. There is also a clear structural relationship between them; the Fe_{22} and Fe_{24} are overall very similar, and the Fe_7 is related to the Fe_8 units at each end of the larger clusters. As is usual in high-nuclearity Fe^{III}/O clusters, there are many bis-monoatomically bridged Fe_2 pairs with resulting weak J_{ij} exchange coupling, and these are completely frustrated by competing strong interactions, leading to Ising-like $m_s = \pm^5/_2$ spin alignments and thus a ready rationalization of the overall ground-state S values for the three clusters. The synergistic use of the polynuclear Fe^{III}/O MSC and DFT methods represents a powerful complement to experimental magnetic studies, providing an overall three-pronged analytical

https://doi.org/10.1021/acs.inorgchem.2c01371
Inorg. Chem. 2022, 61, 11261−11276

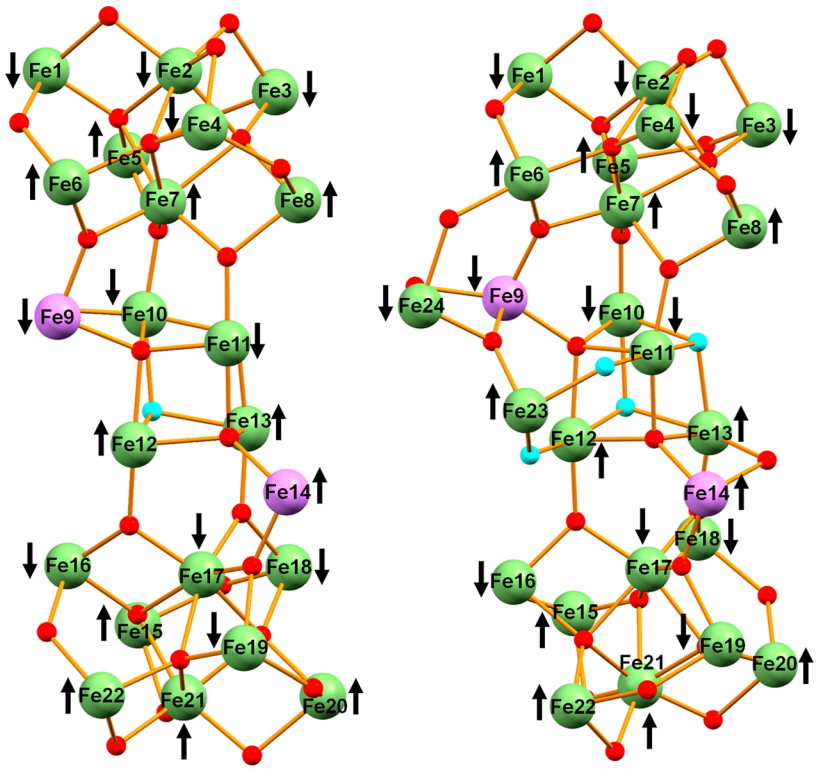

Figure 12. Summary of the ground-state $m_s = \pm^5/_2$ spin alignments for the complete cations of (left) **2** and (right) **3** predicted by both the J_{MSC} and the J_{DFT} values, and also the energy calculations by DFT. Color code: octahedral Fe^{III} lime green, square-pyramidal Fe^{III} lavender, O red, and OH^- sky blue.

approach of great potential for application to a variety of cluster nuclearities and topologies. This is well evidenced in the present work, which has led to a highly satisfying elucidation of the ground-state spin configuration in such high-nuclearity systems. Further studies at even higher Fe_x nuclearities are in progress.

■ ASSOCIATED CONTENT

Supporting Information

The Supporting Information is available free of charge at https://pubs.acs.org/doi/10.1021/acs.inorgchem.2c01371.

Selected bond distances, bond valence sums, RMSD analyses, J_{MSC} and J_{DFT} exchange interactions, various structural figures, g versus D error surface for **1**, and χ_M'' versus T plots for **1**, **2**, and **3** (PDF)

Accession Codes

CCDC 274154, 2163470, and 2163471 contain the supplementary crystallographic data for this paper. These data can be obtained free of charge via www.ccdc.cam.ac.uk/data_request/cif, or by emailing data_request@ccdc.cam.ac.uk, or by contacting The Cambridge Crystallographic Data Centre, 12 Union Road, Cambridge CB2 1EZ, UK; fax: +44 1223 336033.

■ AUTHOR INFORMATION

Corresponding Author

George Christou − *Department of Chemistry, University of Florida, Gainesville, Florida 32611-7200, Unites States;* orcid.org/0000-0001-5923-5523; Phone: +1-352-392-8314; Email: christou@chem.ufl.edu

Authors

Ashlyn R. Hale − *Department of Chemistry, University of Florida, Gainesville, Florida 32611-7200, Unites States;* orcid.org/0000-0001-5120-4693

Megan E. Lott − *Department of Chemistry, University of Florida, Gainesville, Florida 32611-7200, Unites States;* orcid.org/0000-0001-9854-6252

Juan E. Peralta − *Department of Physics and Science of Advanced Materials, Central Michigan University, Mount Pleasant, Michigan 48859, United States*

Dolos Foguet-Albiol − *Department of Chemistry, University of Florida, Gainesville, Florida 32611-7200, Unites States*

Khalil A. Abboud − *Department of Chemistry, University of Florida, Gainesville, Florida 32611-7200, Unites States*

Complete contact information is available at: https://pubs.acs.org/10.1021/acs.inorgchem.2c01371

Notes

The authors declare no competing financial interest.

An anonymous referee analyzed the Fe_7 cluster **1** by employing the irreducible tensor approach. The total number of magnetic states $N = 6^7 = 279{,}936$ in the partition function can be processed using the $M = 24{,}017$ zero-field states. Such a matrix can be divided into blocks of the same molecular spin: for $S = {}^1/_2$ to $S = {}^{35}/_2$, the size of each block is 1050, 1974, 2666, 3060, 3150, 2975, 2604, 2121, 1610, 1140, 750, 455, 252, 126, 56, 21, 6, and 1. Using the four exchange coupling constants J_1−J_4 obtained from the MSC approach (Figure 8), the calculated ground state is $S = {}^5/_2$ separated from an $S = {}^7/_2$ first excited state by 157 cm^{-1} and from the second excited state of a degenerate $S = {}^3/_2$ pair by 190 cm^{-1}. The complete energy spectrum is shown in Figure S11. We thank the referee for

https://doi.org/10.1021/acs.inorgchem.2c01371
Inorg. Chem. 2022, 61, 11261−11276

taking the time to do this and the interest in our work that it reflects, which we take as a very nice compliment.

■ ACKNOWLEDGMENTS

This work was supported by the U.S. National Science Foundation (Grant CHE-1900321) and by the Department of Energy, Office of Science, Office of Basic Energy Sciences as part of the Computational Chemical Sciences Program under award #DE-SC0018331. We thank the NSF for funding of the X-ray diffractometer through grant CHE-1828064. J.E.P. acknowledges support from the Office of Basic Energy Sciences, US Department of Energy, DE-SC0005027.

■ REFERENCES

(1) (a) Seddon, E. J.; Yoo, J.; Folting, K.; Huffman, J. C.; Hendrickson, D. N.; Christou, G. Dinuclear and Hexanuclear Iron(III) Carboxylate Clusters with a Bis(Bipyridine) Ligand: Supramolecular Aggregation of $[Fe_2O_2]$ Units to Give a $[Fe_6O_6]$ Ladder Structure. *J. Chem. Soc., Dalton Trans.* **2000**, *2*, 3640−3648. (b) Vincent, J. B.; Huffman, J. C.; Christou, G.; Li, Q.; Nanny, M. A.; Hendrickson, D. N.; Fong, R. H.; Fish, R. H. Modeling the Dinuclear Sites of Iron Biomolecules: Synthesis and Properties of $Fe_2O(OAc)_2Cl_2(bipy)_2$ and Its use as an Alkane Activation Catalyst. *J. Am. Chem. Soc.* **1988**, *110*, 6898−6900.

(2) (a) Grant, C. M.; Knapp, M. J.; Streib, W. E.; Huffman, J. C.; Hendrickson, D. N.; Christou, G. Dinuclear and Hexanuclear Iron(III) Oxide Complexes with a Bis(Bipyridine) Ligand: A New $[Fe_6(\mu_3\text{-}O)_4]^{10+}$ Core. *Inorg. Chem.* **1998**, *37*, 6065−6070. (b) Zheng, H.; Yoo, S. J.; Münck, E.; Que, L. The Flexible $Fe_2(\mu\text{-}O)_2$ Diamond Core : A Terminal Iron(IV) - Oxo Species Generated from the Oxidation of a Bis(μ -Oxo) Diiron (III) Complex. *J. Am. Chem. Soc.* **2000**, *122*, 3789−3790.

(3) (a) Zang, Y.; Dong, Y.; Que, L.; Kauffmann, K.; Muenck, E. The First Bis(μ-oxo)diiron(III) Complex. Structure and Magnetic Properties of $[Fe_2(\mu\text{-}O)_2(6TLA)_2](ClO_4)_2$. *J. Am. Chem. Soc.* **1995**, *117*, 1169−1170. (b) Boudalis, A. K.; Raptopoulou, C. P.; Terzis, A.; Perlepes, S. P. 2,2′-Bipyrimidine (Bpym) in Iron(III) Carboxylate Chemistry: Preparation and Characterization of $[Fe_2O(O_2CMe)_2(Bpym)_2(H_2O)_2](ClO_4)_2$, and the Influence of Weak Interactions in the Formation of Metal Clusters. *Polyhedron* **2004**, *23*, 1271−1277.

(4) (a) Lee, J. L.; Biswas, S.; Sun, C.; Ziller, J. W.; Hendrich, M. P.; Borovik, A. S. Bioinspired Di-Fe Complexes: Correlating Structure and Proton Transfer over Four Oxidation States. *J. Am. Chem. Soc.* **2022**, *144*, 4559−4571. (b) Zhang, H. T.; Su, X. J.; Xie, F.; Liao, R. Z.; Zhang, M. T. Iron-Catalyzed Water Oxidation: O−O Bond Formation via Intramolecular Oxo−Oxo Interaction. *Angew. Chem., Int. Ed.* **2021**, *60*, 12467−12474.

(5) Zhang, Z.-M.; Yao, S.; Li, Y.-G.; Clérac, R.; Lu, Y.; Su, Z.-M.; Wang, E.-B. Protein-Sized Chiral Fe_{168} Cages with NbO-Type Topology. *J. Am. Chem. Soc.* **2009**, *131*, 14600−14601.

(6) (a) Gorun, S. M.; Lippard, S. J. Magnetostructural Correlations in Magnetically Coupled (μ-Oxo)Diiron(III) Complexes. *Inorg. Chem.* **1991**, *30*, 1625−1630. (b) Weihe, H.; Güdel, H. U. Angular and Distance Dependence of the Magnetic Properties of Oxo-Bridged Iron(III) Dimers. *J. Am. Chem. Soc.* **1997**, *119*, 6539−6543. (c) Werner, R.; Ostrovsky, S.; Griesar, K.; Haase, W. Magneto-structural Correlations in Exchange Coupled Phenoxo-, Alkoxo-, and Hydroxo-Bridged Dinuclear Iron(III) Compounds. *Inorg. Chim. Acta* **2001**, *326*, 78−88.

(7) (a) Ménage, S.; Zang, Y.; Hendrich, M. P.; Que, L. Structure and reactivity of a bis(.mu.-acetato-O,O')diiron(II) complex, [Fe2(O2CCH3)2(TPA)2](BPh4)2. A model for the diferrous core of ribonucleotide reductase. *J. Am. Chem. Soc.* **1992**, *114*, 7786−7792. (b) Herold, S.; Lippard, S. J. Carboxylate-Bridged Diiron(II) Complexes: Synthesis Characterization, and O_2-Reactivity of Models for the Reduced Diiron Centers in Methane Monooxygenase and Ribonucleotide Reductase. *J. Am. Chem. Soc.* **1997**, *119*, 145−156.

(8) Lee, D.; Lippard, S. J. Structural and Functional Models of the Dioxygen-Activating Centers of Non-Heme Diiron Enzymes Ribonucleotide Reductase and Soluble Methane Monooxygenase. *J. Am. Chem. Soc.* **1998**, *120*, 12153−12154.

(9) (a) Toftlund, H.; Murray, K. S.; Zwack, P. R.; Taylor, L. F.; Anderson, O. P. Structural and Electronic Properties of Tetranuclear Iron(III) Pyridylamine Complexes Containing Cofacial Pairs of μ-Oxo-Bis(μ-Acetato)Iron(III) Moieties. Models for Met Hemerythrins. *J. Chem. Soc., Chem. Commun.* **1986**, 191−193. (b) Mauerer, B.; Crane, J.; Schuler, J.; Wieghardt, K.; Nuber, B. A Hemerythrin Model Complex with Catalase Activity. *Angew. Chem., Int. Ed.* **1993**, *32*, 289−291. (c) Arii, H.; Nagatomo, S.; Kitagawa, T.; Miwa, T.; Jitsukawa, K.; Einaga, H.; Masuda, H. A Novel Diiron Complex as a Functional Model for Hemerythrin. *J. Inorg. Biochem.* **2000**, *82*, 153−162.

(10) Coucouvanis, D.; Reynolds, R. A.; Dunham, W. R. Synthesis and Characterization of a New Class of Asymmetric Aqua-Acetate Bridged Dimers. Solid State Molecular Structures of the $[M_2(\mu\text{-}H_2O)(\mu\text{-}OAc)_2(OAc)_3(Py)_2]^-$ Anions (M = Mn (II), Fe (II), Co (II)). A Structural Model for the Fe_2 Site in Methane Monooxygenase. *J. Am. Chem. Soc.* **1995**, *117*, 7570−7571.

(11) (a) Lippard, S. J. Oxo-Bridged Polyiron Centers in Biology and Chemistry. *Angew. Chem., Int. Ed.* **1988**, *27*, 344−361. (b) Sankaralingam, M.; Palaniandavar, M. Diiron(III) Complexes of Tridentate 3N Ligands as Functional Models for Methane Monooxygenases: Effect of the Capping Ligand on Hydroxylation of Alkanes. *Polyhedron* **2014**, *67*, 171−180.

(12) (a) Theil, E. C. Ferritin: Structure, Gene Regulation, and Cellular Function in Animals, Plants, and Microorganisms. *Annu. Rev. Biochem.* **1987**, *56*, 289−315. (b) Theil, E. C.; Matzapetakis, M.; Liu, X. Ferritins: Iron/Oxygen Biominerals in Protein Nanocages. *J. Biol. Inorg Chem.* **2006**, *11*, 803−810.

(13) (a) Weighardt, K.; Pohl, K.; Jibril, I.; Huttner, G. Hydrolysis Products of the Monomeric Amine Complex $(C_6H_{15}N_3)FeCl_3$: The Structure of the Octameric Iron(III) Cation of $\{[(C_6H_{15}N_3)_6Fe_8(\mu_3\text{-}O)_2(\mu_2\text{-}OH)_{12}]Br_7(H_2O)$. *Angew. Chem., Int. Ed.* **1984**, *23*, 77−78. (b) Barra, A.-L.; Debrunner, P.; Gatteschi, D.; Schulz, C. E.; Sessoli, R. Superparamagnetic-like Behavior in an Octanuclear Iron Cluster. *Europhys. Lett.* **1996**, *35*, 133−138.

(14) (a) Barra, A. L.; Caneschi, A.; Cornia, A.; Fabrizi de Biani, F.; Gatteschi, D.; Sangregorio, C.; Sessoli, R.; Sorace, L. Single-Molecule Magnet Behavior of a Tetranuclear Iron(III) Complex. The Origin of Slow Magnetic Relaxation in Iron(III) Clusters. *J. Am. Chem. Soc.* **1999**, *121*, 5302−5310. (b) Boudalis, A. K.; Donnadieu, B.; Nastopoulos, V.; Clemente-Juan, J. M.; Mari, A.; Sanakis, Y.; Tuchagues, J.-P.; Perlepes, S. P. A Nonanuclear Iron(II) Single-Molecule Magnet. *Angew. Chem., Int. Ed.* **2004**, *43*, 2266−2270.

(15) (a) Accorsi, S.; Barra, A.-L.; Caneschi, A.; Chastanet, G.; Cornia, A.; Fabretti, A. C.; Gatteschi, D.; Mortalò, C.; Olivieri, E.; Parenti, F.; Rosa, P.; Sessoli, R.; Sorace, L.; Wernsdorfer, W.; Zobbi, L. Tuning Anisotropy Barriers in a Family of Tetrairon(III) Single-Molecule Magnets with an S = 5 Ground State. *J. Am. Chem. Soc.* **2006**, *128*, 4742−4755. (b) Schlegel, C.; Burzurí, E.; Luis, F.; Moro, F.; Manoli, M.; Brechin, E. K.; Murrie, M.; van Slageren, J. Magnetic Properties of Two New Fe_4 Single-Molecule Magnets in the Solid State and in Frozen Solution. *Chem.—Eur. J.* **2010**, *16*, 10178−10185.

(16) (a) Zhu, Y.-Y.; Yin, T.-T.; Jiang, S.-D.; Barra, A.-L.; Wernsdorfer, W.; Neugebauer, P.; Marx, R.; Dörfel, M.; Wang, B.-W.; Wu, Z.-Q.; Slageren, J. v.; Gao, S. The Solvent Effect in an Axially Symmetric Fe^{III}_4 Single-Molecule Magnet. *Chem. Commun.* **2014**, *50*, 15090−15093. (b) Zhu, Y.-Y.; Cui, C.; Qian, K.; Yin, J.; Wang, B.-W.; Wang, Z.-M.; Gao, S. A Family of Enantiopure Fe^{III}_4 Single Molecule Magnets: Fine Tuning of Energy Barrier by Remote Substituent. *Dalton Trans.* **2014**, *43*, 11897−11907.

(17) (a) Rigamonti, L.; Piccioli, M.; Nava, A.; Malavolti, L.; Cortigiani, B.; Sessoli, R.; Cornia, A. Structure, Magnetic Properties and Thermal Sublimation of Fluorinated Fe_4 Single-Molecule

https://doi.org/10.1021/acs.inorgchem.2c01371
Inorg. Chem. 2022, 61, 11261−11276

Magnets. *Polyhedron* **2017**, *128*, 9−17. (b) Liu, S.; Deng, Y.-F.; Li, C. A.; Chang, X.; Zhang, Y.-Z. A Linear Trinuclear Ferrous Single Molecule Magnet. *Dalton Trans.* **2018**, *47*, 16704−16708. (c) Barman, S. K.; Cano, J.; Lloret, F.; Mukherjee, R. Single-Molecule-Magnet $Fe^{II}_4Fe^{III}_2$ and Antiferromagnetic Fe^{III}_4 Coordination Clusters. *Inorg. Chem.* **2019**, *58*, 8086−8099.

(18) (a) Benelli, C.; Cano, J.; Journaux, Y.; Sessoli, R.; Solan, G. A.; Winpenny, R. E. P. A Decanuclear Iron(III) Single Molecule Magnet: Use of Monte Carlo Methodology to Model the Magnetic Properties. *Inorg. Chem.* **2001**, *40*, 188−189. (b) Goodwill, J. C.; Sessoli, R.; Gatteschi, D.; Wernsdorfer, W.; Powell, A. K.; Heath, S. L. Towards Nanostructured Arrays of Single Molecule Magnets: New Fe_{19} Oxyhydroxide Clusters Displaying High Ground State Spins and Hysteresis. *J. Chem. Soc., Dalton Trans.* **2000**, 1835−1840.

(19) Foguet-Albiol, D.; Abboud, K. A.; Christou, G. High-Nuclearity Homometallic Iron and Nickel Clusters: Fe_{22} and Ni_{24} Complexes from the Use of N-Methyldiethanolamine. *Chem. Commun.* **2005**, *2*, 4282−4284.

(20) Botezat, O.; Van Leusen, J.; Kögerler, P.; Baca, S. G. Tuning the Condensation Degree of $\{Fe^{III}_n\}$ Oxo Clusters via Ligand Metathesis, Temperature, and Solvents. *Inorg. Chem.* **2018**, *57*, 7904−7913.

(21) Dearle, A. E.; Cutler, D. J.; Fraser, H. W. L.; Sanz, S.; Lee, E.; Dey, S.; Diaz-Ortega, I. F.; Nichol, G. S.; Nojiri, H.; Evangelisti, M.; Rajaraman, G.; Schnack, J.; Cronin, L.; Brechin, E. K. An $[Fe^{III}_{34}]$ Molecular Metal Oxide. *Angew. Chem., Int. Ed.* **2019**, *58*, 16903−16906.

(22) (a) Low, D. M.; Jones, L. F.; Bell, A.; Brechin, E. K.; Mallah, T.; Rivière, E.; Teat, S. J.; McInnes, E. J. L. Solvothermal Synthesis of a Tetradecametallic Fe^{III} Cluster. *Angew. Chem., Int. Ed.* **2003**, *42*, 3781−3784. (b) Ako, A. M.; Mereacre, V.; Lan, Y.; Anson, C. E.; Powell, A. K. Combined Use of Magnetic Susceptibility Measurements and Fe Mössbauer Spectroscopy to Determine the Magnetic Ground State of an Fe^{III}_{16} Cluster. *Chem.—Eur. J.* **2011**, *17*, 4366−4370.

(23) (a) Baca, S. G.; Speldrich, M.; Van Leusen, J.; Ellern, A.; Kögerler, P. Undecametallic and Hexadecametallic Ferric Oxo-Hydroxo/Ethoxo Pivalate Clusters. *Dalton Trans.* **2015**, *44*, 7777−7780. (b) Powell, A. K.; Heath, S. L.; Gatteschi, D.; Pardi, L.; Sessoli, R.; Spina, G.; Del Giallo, F.; Pieralli, F. Synthesis, Structures, and Magnetic Properties of Fe_2, Fe_{17}, and Fe_{19} Oxo-Bridged Iron Clusters: The Stabilization of High Ground State Spins by Cluster Aggregates. *J. Am. Chem. Soc.* **1995**, *117*, 2491−2502.

(24) Nachtigall, O.; Kusserow, M.; Clérac, R.; Wernsdorfer, W.; Menzel, M.; Renz, F.; Mrozinski, J.; Spandl, J. Super-Lindqvist" Aggregate and Large 3D Interpenetrating Coordination Polymer from Solvothermal Reactions of $[Fe_2(O^tBu)_6]$ with Ethanol. *Angew. Chem., Int. Ed.* **2015**, *54*, 10361−10364.

(25) (a) Datta, S.; Betancur-Rodriguez, A.; Lee, S.-C.; Hill, S.; Foguet-Albiol, D.; Bagai, R.; Christou, G. EPR Characterization of Half-Integer-Spin Iron Molecule-Based Magnets. *Polyhedron* **2007**, *26*, 2243−2246. (b) Hale, A. R.; Aebersold, L. E.; Foguet-Albiol, D.; Peralta, J. E.; Abboud, K. A.; Christou, G. A multi-pronged approach to molecular spin frustration in a heptanuclear Fe^{III}/oxo complex, manuscript in preparation.

(26) (a) Cañada-Vilalta, C.; O'Brien, T. A.; Brechin, E. K.; Pink, M.; Davidson, E. R.; Christou, G. Large Spin Differences in Structurally Related Fe_6 Molecular Clusters and Their Magnetostructural Explanation. *Inorg. Chem.* **2004**, *43*, 5505−5521. (b) McCusker, J. K.; Vincent, J. B.; Schmitt, E. A.; Mino, M. L.; Shin, K.; Coggin, D. K.; Hagen, P. M.; Huffman, J. C.; Christou, G.; Hendrickson, D. N. Molecular Spin Frustration in the $[Fe_4O_2]^{8+}$ Core: Synthesis, Structure, and Magnetochemistry of $[Fe_4O_2(O_2CR)_7(bpy)_2](ClO_4)$ (R = Me, Ph). *J. Am. Chem. Soc.* **1991**, *113*, 3012−3021. (c) Singh, A. P.; Joshi, R. P.; Abboud, K. A.; Peralta, J. E.; Christou, G. Molecular Spin Frustration in Mixed-Chelate Fe_5 and Fe_6 Oxo Clusters with High Ground State Spin Values. *Polyhedron* **2020**, *176*, 114182.

(27) Gatteschi, D.; Sessoli, R.; Cornia, A. Single-Molecule Magnets Based on Iron(III) Oxo Clusters. *Chem. Commun.* **2000**, 725−732.

(28) Mitchell, K. J.; Abboud, K. A.; Christou, G. Magnetostructural Correlation for High-Nuclearity Iron(III)/Oxo Complexes and Application to Fe_5, Fe_6, and Fe_8 Clusters. *Inorg. Chem.* **2016**, *55*, 6597−6608.

(29) (a) Kitos, A. A.; Papatriantafyllopoulou, C.; Tasiopoulos, A. J.; Perlepes, S. P.; Escuer, A.; Nastopoulos, V. Binding of Ligands Containing Carbonyl and Phenol Groups to Iron(III): New Fe_6, Fe_{10} and Fe_{12} Coordination Clusters. *Dalton Trans.* **2017**, *46*, 3240−3251. (b) Lengyel, J.; Stoian, S. A.; Dalal, N.; Shatruk, M. Directed Synthesis and Magnetic Properties of a Hexanuclear Ferric Cluster. *Polyhedron* **2018**, *151*, 446−451.

(30) (a) Lee, K. H. K.; Peralta, J. E.; Abboud, K. A.; Christou, G. Iron(III)-Oxo Cluster Chemistry with Dimethylarsinate Ligands: Structures, Magnetic Properties, and Computational Studies. *Inorg. Chem.* **2020**, *59*, 18090−18101. (b) Arizaga, L.; Cañon-Mancisidor, W.; Gancheff, J. S.; Burrow, R. A.; Armentano, D.; Lloret, F.; González, R.; Kremer, C.; Chiozzone, R. New Hexanuclear FeIII Clusters with the Gem-Diol Hydrated Form of Di(2-Pyridyl)Ketone and Carboxylato Ligands: Crystal Structures and Magnetic Properties. *Polyhedron* **2019**, *174*, 114165.

(31) Chilton, N. F.; Anderson, R. P.; Turner, L. D.; Soncini, A.; Murray, K. S. PHI: a powerful new program for the analysis of anisotropic monomeric and exchange-coupled polynuclear d- and f-block complexes. *J. Comput. Chem.* **2013**, *34*, 1164−1175.

(32) Earnshaw, A.; Figgis, B. N.; Lewis, J. Chemistry of Polynuclear Compounds. Part VI.* Magnetic Properties of Trimeric Chromium and Iron Carboxylates. *J. Chem. Soc. A* **1966**, 1656−1663.

(33) Sheldrick, G. M. Crystal structure refinement with SHELXL. *Acta Crystallogr., Sect. C: Struct. Chem.* **2015**, *71*, 3−8.

(34) (a) van Wüllen, C. Broken Symmetry Approach to Density Functional Calculation of Magnetic Anisotropy or Zero Field Splittings for Multinuclear Complexes with Antiferromagnetic Coupling. *J. Phys. Chem. A* **2009**, *113*, 11535−11540. (b) Bencini, A.; Totti, F.; Daul, C. A.; Doclo, K.; Fantucci, P.; Barone, V. Density Functional Calculations of Magnetic Exchange Interactions in Polynuclear Transition Metal Complexes. *Inorg. Chem.* **1997**, *36*, 5022−5030.

(35) (a) Ruiz, E.; Rodríguez-Fortea, A.; Cano, J.; Alvarez, S.; Alemany, P. About the calculation of exchange coupling constants in polynuclear transition metal complexes. *J. Comput. Chem.* **2003**, *24*, 982−989. (b) Valero, R.; Costa, R.; de P R Moreira, I.; Truhlar, D. G.; Illas, F. Performance of the M06 family of exchange-correlation functionals for predicting magnetic coupling in organic and inorganic molecules. *J. Chem. Phys.* **2008**, *128*, 114103.

(36) Comba, P.; Hausberg, S.; Martin, B. Calculation of Exchange Coupling Constants of Transition Metal Complexes with DFT. *J. Phys. Chem. A* **2009**, *113*, 6751−6755.

(37) Phillips, J. J.; Peralta, J. E. Magnetic Exchange Couplings from Semilocal Functionals Evaluated Non-self-Consistently on Hybrid Densities: Insights on Relative Importance of Exchange, Correlation, and Delocalization. *J. Chem. Theory Comput.* **2012**, *8*, 3147−3158.

(38) Joshi, R. P.; Phillips, J. J.; Mitchell, K. J.; Christou, G.; Jackson, K. A.; Peralta, J. E. Accuracy of density functional theory methods for the calculation of magnetic exchange couplings in binuclear iron(III) complexes. *Polyhedron* **2020**, *176*, 114194.

(39) (a) Krishnan, R.; Binkley, J. S.; Seeger, R.; Pople, J. A. Self-consistent molecular orbital methods. XX. A basis set for correlated wave functions. *J. Chem. Phys.* **1980**, *72*, 650. (b) Blaudeau, J.-P.; McGrath, M. P.; Curtiss, L. A.; Radom, L. Extension of Gaussian-2 (G2) theory to molecules containing third-row atoms K and Ca. *J. Chem. Phys.* **1997**, *107*, 5016.

(40) Frisch, M. J.; Trucks, G. W.; Schlegel, H. B.; Scuseria, G. E.; Robb, M. A.; Cheeseman, J. R.; Scalmani, G.; Barone, V.; Petersson, G. A.; Nakatsuji, H.; Li, X.; Caricato, M.; Marenich, A. V.; Bloino, J.; Janesko, B. G.; Gomperts, R.; Mennucci, B.; Hratchian, H. P.; Ortiz, J. V.; Izmaylov, A. F.; Sonnenberg, J. L.; Williams-Young, D.; Ding, F.; Lipparini, F.; Egidi, F.; Goings, J.; Peng, B.; Petrone, A.; Henderson, T.; Ranasinghe, D.; Zakrzewski, V. G.; Gao, J.; Rega, N.; Zheng, G.; Liang, W.; Hada, M.; Ehara, M.; Toyota, K.; Fukuda, R.; Hasegawa, J.;

https://doi.org/10.1021/acs.inorgchem.2c01371
Inorg. Chem. 2022, 61, 11261−11276

Ishida, M.; Nakajima, T.; Honda, Y.; Kitao, O.; Nakai, H.; Vreven, T.; Throssell, K.; Montgomery, J. A., Jr.; Peralta, J. E.; Ogliaro, F.; Bearpark, M. J.; Heyd, J. J.; Brothers, E. N.; Kudin, K. N.; Staroverov, V. N.; Keith, T. A.; Kobayashi, R.; Normand, J.; Raghavachari, K.; Rendell, A. P.; Burant, J. C.; Iyengar, S. S.; Tomasi, J.; Cossi, M.; Millam, J. M.; Klene, M.; Adamo, C.; Cammi, R.; Ochterski, J. W.; Martin, R. L.; Morokuma, K.; Farkas, O.; Foresman, J. B.; Fox, D. J. *Gaussian 16*, Revision C.01; Gaussian, Inc.: Wallingford CT, 2016.

(41) Davidson, E. R. *MAGNET*; Indiana University: Bloomington, IN, 1999.

(42) Davidson, E. R. *GRID*; Indiana University, Bloomington, IN, 1999.

(43) Bain, G. A.; Berry, J. F. Diamagnetic Corrections and Pascal's Constants. *J. Chem. Educ.* **2008**, *85*, 532.

(44) Ako, A. M.; Waldmann, O.; Mereacre, V.; Klöwer, F.; Hewitt, I. J.; Anson, C. E.; Güdel, H. U.; Powell, A. K. Odd-Numbered Fe^{III} Complexes: Synthesis, Molecular Structure, Reactivity, and Magnetic Properties. *Inorg. Chem.* **2007**, *46*, 756−766.

(45) (a) Brese, N. E.; O'Keeffe, M. Bond-Valence Parameters for Solids. *Acta Crystallogr., Sect. B: Struct. Sci.* **1991**, *47*, 192−197. (b) Liu, W.; Thorp, H. H. Bond Valence Sum Analysis of Metal-Ligand Bond Lengths in Metalloenzymes and Model Complexes. 2. Refined Distances and Other Enzymes. *Inorg. Chem.* **1993**, *32*, 4102.

https://doi.org/10.1021/acs.inorgchem.2c01371
Inorg. Chem. 2022, 61, 11261−11276